Numerical simulations of seismic cycles in a viscoelastic half-space with the integral method

Sylvain Barbot[1]

[1]Department of Earth Sciences, University of Southern California

Key Points:

- The integral method combines surface and volume elements to simulate seismic cycles in a viscoelastic half-space.
- The method captures the coupling between fault dynamics and viscoelastic processes in the lower crust and asthenosphere.
- Numerical simulations resolve the evolution of surface displacements and quasi-dynamic stress transfer.

Corresponding author: Sylvain Barbot, `sbarbot@usc.edu`

Abstract

Numerical simulations of seismic cycles with rate-, state-, and temperature-dependent friction explain the various modes of seismic and aseismic ruptures in the brittle section of the lithosphere. However, the effects of viscoelastic flow in the ductile layers remain challenging to incorporate due to the wide range of length scales involved, from extremely localized within fault zones to widely distributed in the lower crust and asthenosphere. Here, we describe simulations of seismic cycles in a viscoelastic half-space using the integral method that combines discrete surface and volume elements to capture the coupling between brittle and ductile deformation. Viscoelastic flow is captured by cuboidal and tetrahedral volume elements within rectilinear and curvilinear meshes, respectively. The model resolves all phases of the seismic cycle under the radiation-damping approximation, including the nucleation and propagation of earthquake ruptures, but also the viscoelastic relaxation that follows in the ductile layers. We illustrate the approach in three dimensions with numerical simulations of seismic cycles on finite strike-slip and thrust faults overlying a viscoelastic lower crust with linear and nonlinear rheology. In two-dimensional models of subduction zones with the in-plane strain approximation, the ductile regions are meshed with triangle volume elements. The use of Green's functions only requires the discretization of the actively deforming region, resulting in a relatively small mesh. We provide open-source software implementing the method with parallel computing in a distributed architecture. The approach allows increasingly realistic representations of the lithosphere-asthenosphere system with nonlinear constitutive laws in structurally complex tectonic settings.

Plain Language Summary

Modeling of crustal dynamics during the seismic cycle is important to better understand the genesis of earthquakes and the deformation of Earth's surface. The mechanics of the lithosphere incorporates brittle deformation in the crust and upper mantle, but also viscoelastic flow in the lower crust and asthenosphere. Rapid fault slip during earthquakes induces a sudden stress perturbation in the surrounding lithosphere that is diffused by creep on nearby faults and viscoelastic relaxation at greater depths. These processes continue to deform Earth's surface for decades following large earthquakes. We present a numerical method that captures these phenomena with a consistent description of brittle and ductile deformation. The method is based on a parsimonious representation of faults and distributed plasticity with surface element and volume elements, respectively. We describe numerical simulations based on this method that resolve the nucleation and propagation of earthquakes, but also the afterslip and viscoelastic relaxation that follows. The recurrence time of earthquakes is affected by the rheological properties of the ductile region. The work includes open-source software to explore the mechanics of the seismic cycle in two-dimensional and three-dimensional viscoelastic half-spaces.

1 Introduction

Lithosphere dynamics involves two main types of deformation: localized deformation across faults in the cold, brittle layers and broadly distributed viscoelastic strain in the ductile substrate of the lower crust and asthenosphere [*Kohlstedt et al.*, 1995; *Burov and Watts*, 2006]. The characteristics of seismic cycles are primarily controlled by the nonlinear constitutive properties of faults, which are influenced by temperature, rock composition, and the presence of fluids [*Blanpied et al.*, 1995; *Nakatani*, 2001; *Mitchell et al.*, 2016; *Veedu et al.*, 2020; *Mei et al.*, 2021]. The structural intricacy of fault networks within a plate boundary also plays a significant role [*Romanet et al.*, 2018; *Chen et al.*, 2020; *Gauriau and Dolan*, 2021]. However, additional complexity arises from the mechanical coupling between brittle and ductile deformation that gives rise to quasi-static stress transfer among faults over the interseismic period [*Nur and Mavko*, 1974; *Savage*, 2000; *Freed and Lin*, 2001].

The viscoelastic behavior of the lithosphere is well documented during seismic cycle [e.g., *Bürgmann and Dresen*, 2008; *Pollitz*, 2019]. Following large earthquakes, the lower crust and asthenosphere exhibit accelerated viscoelastic flow due to the sudden stress perturbation caused by the mainshock. Viscoelastic relaxation has been inferred in various tectonic environments, including at continental transforms [*Barbot et al.*, 2008; *Johnson et al.*, 2009; *Pollitz et al.*, 2000, 2001; *Pollitz*, 2003a; *Johnson and Segall*, 2004; *Masuti et al.*, 2016; *Moore et al.*, 2017] and subduction zones [*Hu et al.*, 2004; *Pollitz et al.*, 2006; *Wang*, 2007; *Pollitz et al.*, 2008; *Suito and Freymueller*, 2009; *Wang et al.*, 2012; *Sun et al.*, 2014; *Klein et al.*, 2016; *Qiu et al.*, 2018; *Weiss et al.*, 2019; *Agata et al.*, 2019] after great and giant earthquakes. Typically, modeling approaches consider individual earthquakes as initial condition for postseismic relaxation [*Barbot et al.*, 2009; *Rousset et al.*, 2012; *Rollins et al.*, 2015; *Broerse et al.*, 2015; *Bedford et al.*, 2016; *Li et al.*, 2017; *Diao et al.*, 2018; *Fukuda and Johnson*, 2021], and several numerical methods tackle this initial-value problem efficiently [*Pollitz*, 1992, 1997; *Wang et al.*, 2003; *Pollitz*, 2003b; *Smith and Sandwell*, 2004; *Barbot and Fialko*, 2010a,b; *Hu and Wang*, 2012; *Aagaard et al.*, 2013; *Tanaka et al.*, 2015; *Hampel and Hetzel*, 2015; *Wang et al.*, 2017; *Agata et al.*, 2019; *Nield et al.*, 2022]. However, the nonlinear rheology of the bulk rocks and longer relaxation times compared to earthquake recurrence intervals makes the system sensitive to the history of past deformation [*Ellis and Stöckhert*, 2004; *Hetland and Hager*, 2006; *Nüchter and Ellis*, 2010; *Chuang and Johnson*, 2011; *Takeuchi and Fialko*, 2013].

Viscoelastic deformation also impacts the loading of the seismogenic zone, resulting in first-order changes in earthquake recurrence patterns [e.g., *Allison and Dunham*, 2018; *Barbot*, 2020a; *Shi et al.*, 2020; *Allison and Dunham*, 2021]. At longer time scales, viscoelastic flow plays a crucial role in the transport and recycling of tectonic plates, influencing the rate of slip accumulation on faults at first order at plate boundaries. However, incorporating these important effects is challenging due to the disparity of timescales between mountain building and fault network evolution spanning millions of years, and the seismic cycle operating from milliseconds to centuries. Current models often simplify the rupture process and are limited to two-dimensional representations [*Dinther et al.*, 2013; *Herrendörfer et al.*, 2015; *Biemiller and Lavier*, 2017; *Sobolev and Muldashev*, 2017; *Herrendörfer et al.*, 2018; *Van Zelst et al.*, 2019; *Dal Zilio et al.*, 2019; *Petrini et al.*, 2020].

Integrated models of the lithosphere-asthenosphere system combining brittle and ductile deformation are still elusive because of the wide range of length scales involved and the nonlinear mechanics of faulting and mantle flow. Deformation across faults occurs on a localized scale, spanning from a few centimeters to meters [*Chester and Chester*, 1998; *Mitchell and Faulkner*, 2009; *Faulkner et al.*, 2010]. During a pulse-like rupture, the rupture front can concentrate over hundreds of meters along the fault, which can be significantly smaller than the final slip distribution spanning hundreds of kilometers [*Day*, 1982; *Heaton*, 1990]. Faults are believed to be rooted in deep viscoelastic shear zones several kilometers wide, and the flow of the asthenosphere engages wide regions of the

upper mantle. The constitutive behavior of fault zones is complex, influenced by stress, temperature, and deformation history [*Chester*, 1994; *Blanpied et al.*, 1998; *Niemeijer et al.*, 2016; *Okuda et al.*, 2023]. Similarly, rock rheology may involve a nonlinear behavior due to stress, temperature, water content, and grain size [*Karato and Jung*, 2003; *Hirth and Kohlstedt*, 2003]. Rapid perturbations induce viscoelastic flow with both transient and steady-state responses, making it dependent on strain history [*Chopra*, 1997; *Masuti et al.*, 2016; *Masuti and Barbot*, 2021]. Considering these phenomena, an efficient numerical method that accommodates nonlinear friction and flow laws is needed to resolve the interactions between fault slip and viscoelastic flow during seismic cycles in a three-dimensional half-space.

The boundary integral method offers key advantages for simulating seismic cycles, resolving stress interactions among faults analytically using Green's functions [*Andrews*, 1985; *Day et al.*, 2005; *Chen and Zhang*, 2006; *Lapusta and Liu*, 2009; *Tada*, 2009; *Ando*, 2016; *Barbot*, 2021; *Romanet and Ozawa*, 2022] instead of relying on numerical meshes of the surrounding volume, as done in the finite-element method [*Aagaard et al.*, 2013]. The dimension reduction of the numerical model strongly reduces the computational burden. Various analytical solutions for displacement and stress caused by surface elements are readily available to represent a displacement discontinuity embedded within an elastic half-space [*Comninou and Dundurs*, 1975; *Okada*, 1992; *Meade*, 2007; *Gimbutas et al.*, 2012; *Nikkhoo and Walter*, 2015]. A combination of rectangle and triangle surface elements can be used to shape realistic, non-planar fault geometries [e.g., *Hori et al.*, 2004; *Qiu et al.*, 2016; *Li and Liu*, 2017; *Shibazaki et al.*, 2019; *Perez-Silva et al.*, 2022]. The use of analytic solutions ensures high accuracy in simulating surface displacements by resolving the free surface exactly [*Qiu et al.*, 2016; *Wang and Barbot*, 2020; *Sathiakumar and Barbot*, 2021]. However, the boundary integral method, as applied to an elastic half-space, is currently limited to representing fault dynamics. Ongoing efforts are focused on including viscoelastic processes in a full space to study earthquake source processes [*Miyake and Noda*, 2019; *Noda*, 2022], ignoring lateral variations of viscoelastic properties, nonlinear flow laws, and the effect of the free surface. Resolving the free surface is paramount for geodetic applications because this is where measurements are made. Other studies based on the finite-element or finite-difference methods capture nonlinear viscoelastic properties and thermal effects, but are limited to two-dimensional, anti-plane strain [*Zhang and Sagiya*, 2018; *Allison and Dunham*, 2021]. A semi-analytic method to investigate the impact of brittle and ductile deformation on crustal dynamics during seismic cycles in a three-dimensional half-space is still missing.

The boundary integral method focuses on resolving interactions among surface elements. The method is particularly suited for capturing the nonlinear dynamics of fault processes, including slow-slip events, earthquakes, and other frictional instabilities [*Shibazaki and Shimamoto*, 2007; *Shibazaki et al.*, 2011; *Barbot et al.*, 2012; *Dublanchet et al.*, 2013; *Dublanchet*, 2017; *Nie and Barbot*, 2021, 2022; *Wang and Barbot*, 2023a, and references therein]. The surface elements represent displacement discontinuities within the half-space, capturing the localized deformation associated with faulting. The corresponding Green's functions describe the displacement and stress in the surrounding rocks. The method can be extended naturally by incorporating volume elements to accommodate distributed anelastic deformation (Figure 1). The volume elements represent a concentration of anelastic strain due to crystal plasticity. Similar Green's functions describe the resulting displacement and stress in the surrounding medium [*Barbot et al.*, 2017; *Barbot*, 2018a, 2020b]. Combining these features within the integral method enables the coupling between brittle and ductile deformation within the lithosphere. The approach provides a unified representation of the lithosphere-asthenosphere system, capturing the dynamics of faults and the evolution of distributed plastic deformation. The use of Green's functions allows the simulation of surface displacements to compare with geodetic data [e.g., *Qiu et al.*, 2018; *Weiss et al.*, 2019; *Barbot and Weiss*, 2021; *Wang and Barbot*, 2023b]. The integral method has been developed for two-dimensional viscoelastic half-spaces under

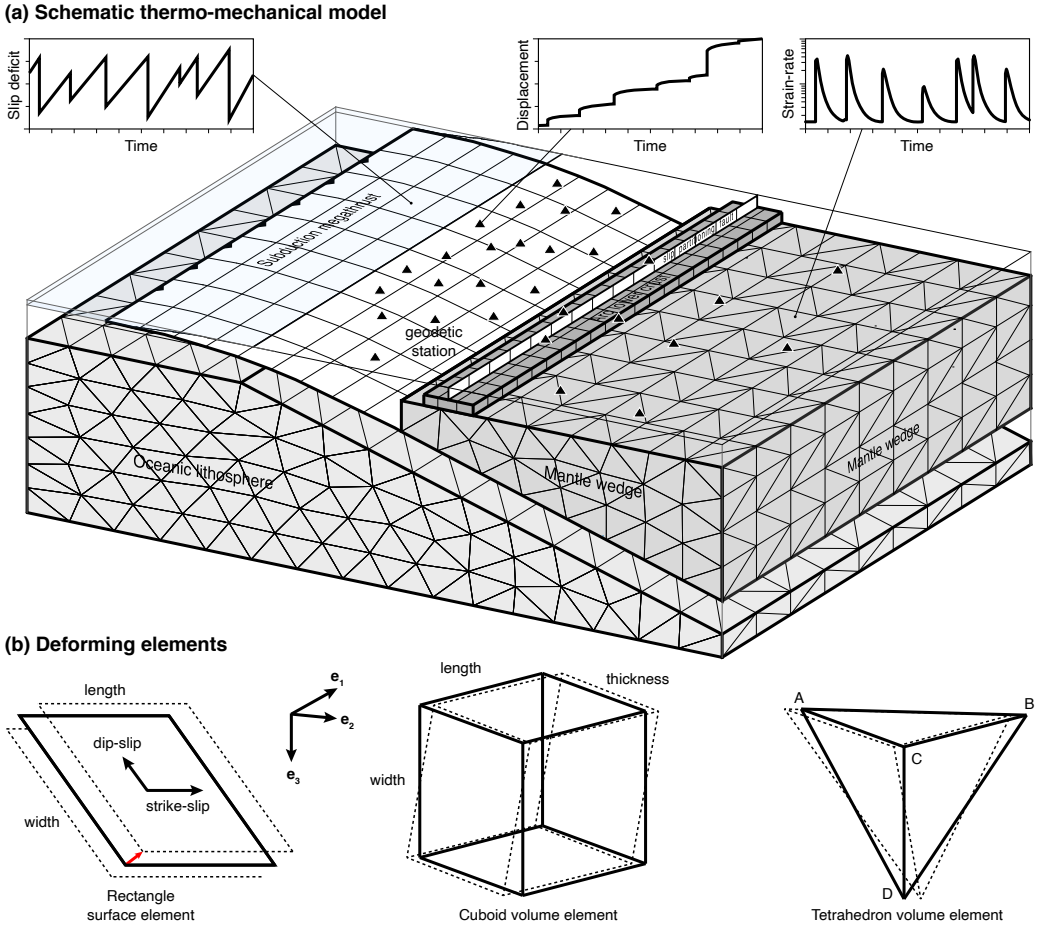

Figure 1: Schematic representation of the integral method combining surface and volume elements to capture the mechanical coupling between fault slip and viscoelastic flow. a) The approach is illustrated for the case of a subduction zone with a megathrust and slip-partitioning strike-slip fault along a volcanic arc. The faults are meshed with rectangle surface elements. The viscoelastic substrate is meshed with volume elements. Here, we use tetrahedral elements in the oceanic lithosphere and mantle wedge, and cuboidal elements in the arc lower crust. Green's functions are used to track the evolution of stress and surface tractions on volume and surface elements, respectively, allowing simulation of seismic cycles. Sequences of earthquakes and slow-slip events are followed by viscoelastic relaxation in the ductile substrate, which affects the recurrence times of future events. Different Green's functions are used to simulate crustal deformation at geodetic stations (triangles). b) Types of plastically deforming elements considered in the study. Rectangle surface elements represent fault slip. Cuboidal and tetrahedral volume elements can be used to build rectilinear and curvilinear meshes, respectively.

the anti-plane [*Lambert and Barbot*, 2016] and in-plane [*Barbot*, 2018b; *Shi et al.*, 2020; *Barbot*, 2020a] strain approximations, as well as for a three-dimensional viscoelastic half-space [*Shi et al.*, 2022]. However, a numerically stable method that can capture structural complexity and nonlinear constitutive laws using open-source software is insofar unavailable.

In this paper, we present a stable implementation of the integral method that combines surface and volume elements to simulate fault dynamics in a viscoelastic half-space during all phases of the seismic cycle. The method incorporates nonlinear constitutive laws and can handle complex structural settings with lateral variations of rock properties. In the following sections, we describe the integral method to simulate lithosphere dynamics within a three-dimensional viscoelastic half-space, utilizing cuboidal and tetrahedral elements to represent the viscoelastic layers. We illustrate the method with three-dimensional simulations of seismic cycles along strike-slip and thrust faults using rectilinear and curvilinear meshes for the viscoelastic substrate. Subsequently, we explain the application of the method in two-dimensional systems under the in-plane strain approximation. We demonstrate how triangle volume elements can conform to the complex structural setting of a megathrust overlying a subducting oceanic lithosphere and an overturning mantle wedge. We provide open-source software in a companion paper to facilitate the use of the proposed methodology [*Barbot*, submitted]. The integral method provides an effective tool to create realistic models of lithosphere dynamics and crustal deformation, bridging the fields of rupture dynamics, tectonic geodesy, and rock mechanics.

2 The integral method

2.1 Elastic-plastic decomposition

Our goal is to incorporate different mechanisms of deformation distributed throughout the lithosphere to integrate their mechanical coupling and describe their relative contribution to surface displacement (Figure 1). During seismic cycles, the source of deformation is often deeply buried, either along a blind fault or below the confines of the brittle-crust. Surface displacements result from the elastic coupling with these distant sources. To represent deformation originating from different types of sources, it is useful to consider the elastic and anelastic decomposition of the total strain-rate tensor, as in

$$\dot{\epsilon}_{ij} = \dot{\epsilon}^e_{ij} + \dot{\epsilon}^p_{ij} \ , \tag{1}$$

where $\dot{\epsilon}^e_{ij}$ represents the elastic part of the deformation, $\dot{\epsilon}^p_{ij}$ is the anelastic component, the dot representing a rate of change, and we use the index notation with Einstein's summation convention. We assume strain to be infinitesimal. The total strain-rate is the symmetric part of the velocity gradient tensor, as in

$$\dot{\epsilon}_{ij} = \frac{1}{2}\left(\dot{u}_{i,j} + \dot{u}_{j,i}\right) \ , \tag{2}$$

where $\dot{u}_i$ is the velocity field and the subscript comma followed by an index indicates a partial derivative with respect to that coordinate. In this article, we consider the terms anelastic and plastic to be equivalent, representing a thermodynamically irreversible deformation process. Within our assumptions, elastic deformation occurs in response to plastic strain and the current plastic strain represents a point of local thermodynamic equilibrium.

In a faulted viscoelastic medium, anelastic deformation can occur by slip on faults or viscoelastic flow in ductile domains. Viscoelasticity typically involves the deviatoric stress tensor, defined as

$$\sigma'_{ij} = \sigma_{ij} - \frac{\sigma_{kk}}{3}\delta_{ij} \ , \tag{3}$$

where σ_{ij} represent the Cauchy stress tensor and we use the Kronecker delta δ_{ij}. At steady-state, viscoelastic flow obeys a constitutive law for non-Newtonian fluids of the form

$$\dot{\epsilon}^p_{ij} = A\tau^{n-1}\sigma'_{ij} \ , \tag{4}$$

where the scalar $\tau = \sigma'_{ij}\sigma'_{ij}$ is the norm of the deviatoric stress tensor, and A and n are the constitutive parameters encompassing the grain size, water content, and thermal effects. For fault slip, the plastic strain-rate depends on the fault orientation and the local slip-rate as

$$\dot{\epsilon}^p_{ij} = \frac{1}{2}\left(v_i\, n_j + n_i\, v_j\right)\delta(\mathbf{x}-\mathbf{y})\,, \tag{5}$$

where $\delta(\mathbf{x})$ is Dirac's delta function with the physical units of a wavelength indicating intense strain localization along the fault at position $\mathbf{y}$, $\mathbf{v}$ is the slip velocity vector, and $\mathbf{n}$ is the unit normal vector. The instantaneous slip-rate obeys an anisotropic constitutive relationship of the form

$$v_i = v_i(\boldsymbol{\sigma}, \mathbf{n}, \theta, p)\,, \tag{6}$$

where θ is a state variable and p is the pore-fluid pressure. The traction along the fault can be decomposed into the normal and shear components $\mathbf{t}^n$ and $\mathbf{t}^s$, respectively. The velocity of sliding is aligned with the direction of shear traction such that $\mathbf{v}\times\mathbf{t}^s = 0$ at all times, where the operator $\times$ is the vector cross product. The amplitude of slip-rate follows a rate- and state-dependent friction law of the form $V = V(\tau_s, \sigma_n, \theta, p)$, where τ_s and σ_n are the norms of the shear and normal traction vectors, respectively.

The elastic and anelastic decomposition of deformation generalizes the representation theorem for fault slip [*Aki and Richards*, 1980; *Zhang and Chen*, 2006] to include distributed plastic deformation [*Nemat-Nasser and Hori*, 1999; *Nemat-Nasser*, 2004]. As described above, the plastic strain-rate is well defined at any time given the ambient stress and potential state variables. The remaining task is to evaluate the overall velocity field induced by plastic deformation due to elastic coupling. Stress forms when the total strain deviates from the anelastic strain. Hooke's law

$$\sigma_{ij} = C_{ijkl}\epsilon^e_{kl}\,, \tag{7}$$

where C_{ijkl} represents the components of the fourth-order elastic moduli tensor, provides the relationship

$$\dot{\sigma}_{ij} = C_{ijkl}\left(\dot{\epsilon}_{kl} - \dot{\epsilon}^p_{kl}\right)\,, \tag{8}$$

where we assume temporally constant elastic moduli. Equation (8) explains how elastic deformation results from plastic deformation, which introduces the torque

$$\dot{m}_{ij} = C_{ijkl}\dot{\epsilon}^p_{kl} \tag{9}$$

in the system. Conservation of linear momentum for quasi-static equilibrium, neglecting the contribution of seismic waves, can be written

$$\left(C_{ijkl}\dot{\epsilon}_{kl}\right)_{,j} + \dot{f}_i = 0\,, \tag{10}$$

where the forcing term $\dot{f}_i = -\dot{m}_{ji,j}$ is an equivalent body-force representing the effect of plastic deformation. In this study, we consider isotropic elasticity associated with the elastic moduli tensor

$$C_{ijkl} = \lambda\,\delta_{ij}\delta_{kl} + \mu\left(\delta_{ik}\delta_{jl} + \delta_{il}\delta_{jk}\right)\,, \tag{11}$$

where λ and μ are the Lamé parameters with the rigidity μ, both assumed spatially uniform within the half-space. Using the strain-versus-displacement relationship of Equation (2) and the elastic moduli tensor of Equation (11), the governing equation for the velocity field induced by plastic deformation becomes

$$(\lambda+\mu)\,\dot{u}_{j,ij} + \mu\,\dot{u}_{i,jj} + \dot{f}_i = 0\,. \tag{12}$$

Equation (12) under a free-surface boundary condition can be solved in three dimensions using a variety of techniques involving Fourier transforms [*Barbot and Fialko*, 2010a,b], finite difference [*Landry and Barbot*, 2016; *Erickson et al.*, 2017; *Landry and Barbot*, 2018; *Allison and Dunham*, 2021], finite elements [*Aagaard et al.*, 2013], and spectral elements [*Komatitsch and Vilotte*, 1998].

To frame the governing equation compatible with the integral method, we can write Equation (12) in integral form, as in

$$\dot{u}_i(\mathbf{x}) = \iiint G_{ji}(\mathbf{x}, \mathbf{y})\, \dot{f}_j(\mathbf{y})\, \mathrm{d}\mathbf{y} \,, \tag{13}$$

where $G_{ji}(\mathbf{x}, \mathbf{y})$ is the Green's function for the displacement in the direction i caused by a traction in the direction j in an elastic half-space, which is available in closed form [*Mindlin*, 1936; *Press*, 1965; *Okada*, 1985; *Segall*, 2010] and is shown in the Appendix. Solving for the velocity field is important to build time series of crustal deformation. However, inspection of the constitutive laws for plasticity, such as Equations (4) and (6), shows that only stress is required to evaluate the progression of the mechanical system. Per Equations (2) and (8), stress evolution results from a linear combination of the velocity gradient and the plastic strain-rate. Conveniently, the velocity gradient can be directly obtained via Green's functions, as in

$$\dot{u}_{i,j} = \iiint G_{ki,j}(\mathbf{x}, \mathbf{y})\, \dot{f}_k(\mathbf{y})\, \mathrm{d}V \,, \tag{14}$$

involving derivatives of the Green's function for a half-space, also shown in the Appendix. Given the velocity gradient in Equation (14), the total strain-rate tensor can be evaluated with Equation (2). As the current plastic strain-rate is given, the elastic strain-rate and the corresponding rate of change of stress can be evaluated with Equation (8). Therefore, Equation (14) provides key information to track the evolution of the system.

These considerations provide a path toward a unified method to simulate crustal deformation during seismic cycles using the integral method. Given an initial stress field, a plastic strain-rate can be identified using Equations (4) and (5). The corresponding velocity gradient can be obtained with Equation (14), from which a rate of stress can be calculated using Equation (8). Integrating the rate of change of stress at time t using a numerical quadrature provides a new state at time $t + \Delta t$ and the previous steps can be repeated to build time-series. Assuming infinitesimal strain and temporally constant elastic moduli allows us to use the same Green's function throughout the simulation.

The elastic and anelastic decomposition of deformation constitutes an important theoretical underpinning of the integral method, allowing us to incorporate different types of plastic deformation with various degrees of localization into the model. The next step is to establish a numerically efficient procedure to evaluate the convolution operation of Equation (14), which is a computational bottleneck. We will show in the next section how surface and volume elements can be used to capture localized and distributed deformation and to convert Equation (14) into an algebraic expression.

2.2 Surface and volume elements

We consider procedures to track the evolution of stress in the ductile regions and the simultaneous evolution of surface traction along faults, so that constitutive laws such as Equations (4) and (6) can provide the instantaneous plastic strain-rate and slip-rate, respectively. We assume that plastic deformation occurs within a domain Ω and that fault slip localizes along the embedded surface Σ. As the numerical solution involves Green's functions, the stress change is immediately accessible by taking linear combinations of the velocity gradient, following Equation (8). The change of stress in the half-space is caused by flow in nearby regions and by slip on neighboring faults. This can be written

$$\dot{\sigma}_{ij} = \iint_{\Sigma} J_{ijk}(v_k - v_k^L)\, \mathrm{d}A + \iiint_{\Omega} L_{ijkl}(\dot{\epsilon}_{kl}^p - \dot{\epsilon}_{kl}^L)\, \mathrm{d}V \,, \tag{15}$$

where $\dot{\sigma}_{ij}$ can be evaluated anywhere in the half-space, $\dot{\epsilon}_{kl}^p$ and $\dot{\epsilon}_{kl}^L$ are the instantaneous and background plastic strain-rate tensors, and v_k and v_k^L are the fault instantaneous and long-term slip-rate vectors. The background loading corresponds to the asymptotic rate

of deformation and a state of quasi-static equilibrium. The Green's function J_{ijk} is a third-order tensor connecting fault slip and stress that incorporates the local orientation of faults. The Green's function L_{ijkl} is a forth-order tensor connecting plastic strain and stress. Potentially, any component of plastic strain induces change in all components of the stress tensor.

Similarly, the change of surface traction along faults originates from slip on nearby faults and from plastic flow in the ductile domain. For rapid fault slip, a radiation damping term is necessary to account for the outward radiation of energy, which reduces the local stress. Including the so-called radiation-damping approximation [*Rice and Tse*, 1986], the evolution of surface traction can be written

$$\dot{t}_i(\mathbf{x}) = \iint_{\Sigma} K_{ij}(v_j - v_j^L)\,\mathrm{d}A + \iiint_{\Omega} M_{ikl}(\dot{\epsilon}_{kl}^p - \dot{\epsilon}_{kl}^L)\,\mathrm{d}V - \frac{\mu}{2V_S}\dot{v}_i \ , \tag{16}$$

where t_i is the surface traction anywhere along the faulted domain Σ, K_{ij} is a second-order Green's function connecting fault slip to surface traction, M_{ikl} is a third-order Green's function connecting plastic strain to surface traction, μ is the rigidity of rocks surrounding the fault, and V_S is the shear-wave speed. As they produce surface traction, the Green's functions K_{ij} and M_{ikl} incorporate information about the fault orientation. The Green's functions J_{ijk}, L_{ijkl}, K_{ij}, and M_{ikl} can be obtained by linear combinations of G_{ji} and $G_{ji,j}$. However, we will not evaluate the integrals in Equations (15) and (16) directly. Instead, we will resolve to discrete approximations.

We consider a discretization of the deforming domain with a mesh combining surface and volume elements approximating the geometry of faults and the viscoelastic substrate, respectively (Figure 1). We assume uniform slip and plastic strain distribution within surface and volume elements, respectively. Hence, the distribution of slip and plastic strain in the respective domains is piece-wise uniform. For the discretization of fault surfaces, we adopt rectangle elements. For the plastic domain, we utilize cuboidal and tetrahedral elements. However, the following discussion is independent of the discretization scheme. Assuming a proper discretization, Equations (15) and (16) become algebraic. The change of traction and stress anywhere in the half-space results from a linear combination of slip-rate and plastic strain-rate in the surface and volume elements. The evolution of stress in volume elements can be written with the following algebraic expression involving matrix-vector multiplications

$$\dot{\mathbf{S}}_{ij} = \mathbf{J}_{ijk}(\mathbf{V}_k - \mathbf{V}_k^L) + \mathbf{L}_{ijkl}(\mathbf{E}_{kl} - \mathbf{E}_{kl}^L) \tag{17}$$

where $\mathbf{S}_{ij}$ is a vector containing a representative value of the stress component ij for all volume elements in the mesh, $\mathbf{V}_k$ and $\mathbf{V}_k^L$ are vectors describing the k component of instantaneous and background slip-rates, respectively, of all surface elements, and $\mathbf{E}_{kl}$ and $\mathbf{E}_{kl}^L$ are vectors containing the kl component of instantaneous and background plastic strain-rates, respectively. The matrices $\mathbf{J}_{ijk}$ and $\mathbf{L}_{ijkl}$ convert slip in the direction k and plastic strain in the direction kl to stress in the direction ij, respectively. We use a similar discrete approximation for the evolution of traction, giving rise to

$$\dot{\mathbf{T}}_i = \mathbf{K}_{ij}(\mathbf{V}_j - \mathbf{V}_j^L) + \mathbf{M}_{ikl}(\mathbf{E}_{kl} - \mathbf{E}_{kl}^L) - \frac{G}{2V_S}\dot{\mathbf{V}}_i \ , \tag{18}$$

where $\mathbf{T}_i$ is a vector containing the traction component i of all the surface elements, and the matrices $\mathbf{K}_{ij}$ and $\mathbf{M}_{ikl}$ convert fault slip in the direction j and plastic strain in the direction kl to surface traction in the direction i, respectively.

We write the evolution equations more compactly by defining vectors that fully describe all components of deformation, stress, and traction. The velocity vector

$$\mathbf{V} = \begin{pmatrix} \mathbf{V}_1 \\ \mathbf{V}_2 \end{pmatrix} \tag{19}$$

contains the fault slip-rate expressed in a fault-centric coordinate system where $\mathbf{V}_1$ and $\mathbf{V}_2$ represent slip-rate in the strike-parallel and up-dip directions, respectively. The plastic

strain-rate vector

$$\mathbf{E} = \begin{pmatrix} \mathbf{E}_{11} \\ \mathbf{E}_{12} \\ \mathbf{E}_{13} \\ \mathbf{E}_{22} \\ \mathbf{E}_{23} \\ \mathbf{E}_{33} \end{pmatrix} \tag{20}$$

regroups the six independent components of the symmetric plastic strain-rate tensor for all volume elements. For the stress, we define the vector

$$\mathbf{S} = \begin{pmatrix} \mathbf{S}_{11} \\ \mathbf{S}_{12} \\ \mathbf{S}_{13} \\ \mathbf{S}_{22} \\ \mathbf{S}_{23} \\ \mathbf{S}_{33} \end{pmatrix} \tag{21}$$

with the six independent components, taking advantage of the symmetry of the stress tensor that emerges from conservation of angular momentum. Finally, we define a vector of traction components, as

$$\mathbf{T} = \begin{pmatrix} \mathbf{T}_1 \\ \mathbf{T}_2 \\ \mathbf{T}_3 \end{pmatrix} \tag{22}$$

that combines the three components of surface traction expressed in a fault-centric coordinate system, whereby $\mathbf{T}_1$, $\mathbf{T}_2$, and $\mathbf{T}_3$ represent the traction components in the strike-parallel, up-dip, and normal directions, respectively. We keep track of the shear and normal components of surface traction because they both affect fault slip-rate when friction is involved. Given these definitions, we can write stress and traction interaction matrices that couple all components of deformation. The matrix of self-stress interaction in the ductile domain becomes

$$\mathbf{L} = \begin{bmatrix} \mathbf{L}_{1111} & \mathbf{L}_{1112} & \mathbf{L}_{1113} & \mathbf{L}_{1122} & \mathbf{L}_{1123} & \mathbf{L}_{1133} \\ \mathbf{L}_{1211} & \mathbf{L}_{1212} & \mathbf{L}_{1213} & \mathbf{L}_{1222} & \mathbf{L}_{1223} & \mathbf{L}_{1233} \\ \mathbf{L}_{1311} & \mathbf{L}_{1312} & \mathbf{L}_{1313} & \mathbf{L}_{1322} & \mathbf{L}_{1323} & \mathbf{L}_{1333} \\ \mathbf{L}_{2211} & \mathbf{L}_{2212} & \mathbf{L}_{2213} & \mathbf{L}_{2222} & \mathbf{L}_{2223} & \mathbf{L}_{2233} \\ \mathbf{L}_{2311} & \mathbf{L}_{2312} & \mathbf{L}_{2313} & \mathbf{L}_{2322} & \mathbf{L}_{2323} & \mathbf{L}_{2333} \\ \mathbf{L}_{3311} & \mathbf{L}_{3312} & \mathbf{L}_{3313} & \mathbf{L}_{3322} & \mathbf{L}_{3323} & \mathbf{L}_{3333} \end{bmatrix} \tag{23}$$

where the $\mathbf{L}_{ijkl}$ are defined in Equation (17). The matrix of self-stress interaction for faulting is written

$$\mathbf{K} = \begin{bmatrix} \mathbf{K}_{11} & \mathbf{K}_{12} \\ \mathbf{K}_{21} & \mathbf{K}_{22} \\ \mathbf{K}_{31} & \mathbf{K}_{32} \end{bmatrix} \tag{24}$$

where the $\mathbf{K}_{ij}$ are described in Equation (18). The two directions of coupling between fault slip and plastic flow are described by the matrices of stress interactions

$$\mathbf{J} = \begin{bmatrix} \mathbf{J}_{111} & \mathbf{J}_{112} \\ \mathbf{J}_{121} & \mathbf{J}_{122} \\ \mathbf{J}_{131} & \mathbf{J}_{132} \\ \mathbf{J}_{221} & \mathbf{J}_{222} \\ \mathbf{J}_{231} & \mathbf{J}_{232} \\ \mathbf{J}_{331} & \mathbf{J}_{332} \end{bmatrix} \tag{25}$$

and

$$\mathbf{M} = \begin{bmatrix} \mathbf{M}_{111} & \mathbf{M}_{112} & \mathbf{M}_{113} & \mathbf{M}_{122} & \mathbf{M}_{123} & \mathbf{M}_{133} \\ \mathbf{M}_{211} & \mathbf{M}_{212} & \mathbf{M}_{213} & \mathbf{M}_{222} & \mathbf{M}_{223} & \mathbf{M}_{233} \\ \mathbf{M}_{311} & \mathbf{M}_{312} & \mathbf{M}_{313} & \mathbf{M}_{322} & \mathbf{M}_{323} & \mathbf{M}_{333} \end{bmatrix} \tag{26}$$

where the matrices $\mathbf{J}_{ijk}$ and $\mathbf{M}_{ikl}$ are described in Equations (17) and (18), respectively. The matrix $\mathbf{J}$ describes how plastic deformation can be triggered by fault slip. The matrix $\mathbf{M}$ describes how distributed plasticity can induce stress on faults by affecting the

shear and normal traction. With this book keeping, we can write the evolution of stress and traction due to fault slip and plastic flow as

$$\begin{aligned}\dot{\mathbf{S}} &= \mathbf{J}\,(\mathbf{V} - \mathbf{V}^L) + \mathbf{L}\,(\mathbf{E} - \mathbf{E}^L)\\ \dot{\mathbf{T}} &= \mathbf{K}\,(\mathbf{V} - \mathbf{V}^L) + \mathbf{M}\,(\mathbf{E} - \mathbf{E}^L) - \gamma\dot{\mathbf{V}}\ ,\end{aligned} \tag{27}$$

where the vectors $\mathbf{V}^L$ and $\mathbf{E}^L$ contain the long-term deformation for all surface and volume elements, respectively, and $\gamma = \mu/2V_S$ is the radiation damping factor. Equation (27) forms the basis of the integral method where the mechanical coupling among and between surface and volume elements is captured by a series of matrix-vector multiplications that approximate the respective surface and volume integrals. Evaluating Equation (27) constitutes the bulk of the numerical burden with the integral method, as the other operations are local. However, the matrix-vector formulation can be parallelized using shared and distributed memory, relegated to a dedicated computing device, or accelerated with hierarchical matrices [e.g., *Bradley*, 2014; *Ozawa et al.*, 2023]. The Green's function matrices $\mathbf{J}$, $\mathbf{L}$, $\mathbf{K}$, and $\mathbf{M}$ can be used in subsequent simulations based on the same geometry, as changing the frictional or rheological parameters does not affect the Green's functions. How to evaluate the stress caused by moving faults in a half-space is well known [*Okada*, 1992; *Nikkhoo and Walter*, 2015]. We describe next how to calculate the stress induced by plastically deforming volume elements.

2.3 Distributed plastic deformation

The governing equations, written in strong form in Equation (12) or in integral form in Equation (13), involve linear operators. Hence, the principle of superposition applies to evaluate stress interactions, regardless of the nonlinear character of the constitutive equations for plasticity that unfolds in the time domain. Accordingly, we focus on the stress field induced by a single plastically deforming volume element identified by the domain Ω. The stress caused by other elements can be added linearly. To simplify the expressions, we consider displacement, strain, and stress instead of the respective time derivatives. The plastic strain is associated with the moment density m_{ij} inside Ω. The resulting displacement gradient in the half-space can be obtained using the convolution in Equation (14) using the body-force $f_i = m_{ji,j}$ within the volume. However, as the plastic strain is piece-wise uniform, integration by part removes an integral and the stress field can be obtained by a convolution with the equivalent traction at the boundary of the volume [*Barbot*, 2018a]. As a result, the displacement gradient can be obtained with the surface integral

$$u_{i,j} = \int_{\partial\Omega} G_{ji,j} m_{jk} n_k \,\mathrm{d}A\ , \tag{28}$$

where $\partial\Omega$ is the boundary of the volume element and n_k is the k component of the outward-pointing unit normal vector. We evaluate the surface integral in Equation (28) using a numerical quadrature. We consider cuboids and tetrahedra as end-member types of volume elements associated with rectilinear and curvilinear meshes.

For cuboids, the surface integral is conducted on six rectangular faces. We consider a cuboid centered at $\mathbf{y}^s$ with dimensions of length L_1, width L_2, and thickness L_3. The orientation of the cuboid is defined by the right-handed coordinate system aligned with the faces with unit vectors $\mathbf{e}'_1$, $\mathbf{e}'_2$, and $\mathbf{e}'_3$. The primed volume-centric coordinate system relates to the unprimed reference system by a rotation matrix, such that $\mathbf{e}'_i = R_{ij}\mathbf{e}_j$. Using a Gauss-Legendre quadrature of degree N involving the weights w_k and abscissas x_k for $k = 1..N$ [*Press et al.*, 1992], the surface integral of Equation (28) can be approximated by

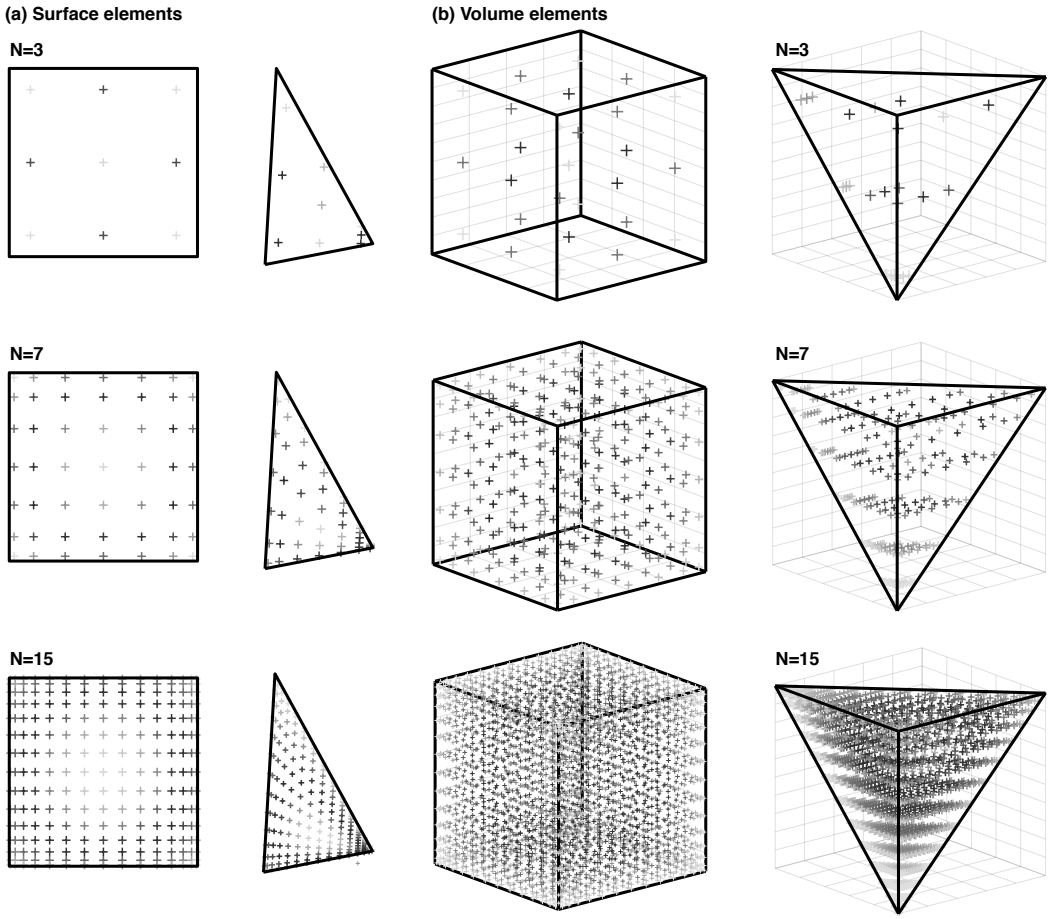

Figure 2: Integration points of the Gauss-Legendre quadrature for surface and volume elements used in calculation of stress and traction caused by plastically deforming volume elements and average stress at receiver volume element. a) Rectangle and triangle faces of cuboidal and tetrahedral volume elements. The integration points (crosses) for quadrature orders $N = 3$, $N = 7$, and $N = 15$ concentrating near the edges of the surface. Regardless of quadrature order, there is no integration point on the edges. b) Integration points for volume integration to select a representative stress within volume elements. The integration points are colored by weight, which are higher toward the center of the faces and volumes.

$$
\begin{aligned}
u_{i,j}(\mathbf{x}) \approx & \frac{L_2 L_3}{4} \sum_{s=1}^{N} \sum_{t=1}^{N} w_s w_t \, G_{ki,j}[\mathbf{x}; \mathbf{y}(\tilde{x}_r, \tilde{x}_s, \tilde{x}_t)] \, m_{kl} R_{1l} \Big|_{\tilde{x}_r=-1}^{\tilde{x}_r=+1} \\
& + \frac{L_1 L_3}{4} \sum_{r=1}^{N} \sum_{t=1}^{N} w_r w_t \, G_{ki,j}[\mathbf{x}; \mathbf{y}(\tilde{x}_r, \tilde{x}_s, \tilde{x}_t)] \, m_{kl} R_{2l} \Big|_{\tilde{x}_s=-1}^{\tilde{x}_s=+1} \\
& + \frac{L_1 L_2}{4} \sum_{r=1}^{N} \sum_{s=1}^{N} w_r w_s \, G_{ki,j}[\mathbf{x}; \mathbf{y}(\tilde{x}_r, \tilde{x}_s, \tilde{x}_t)] \, m_{kl} R_{3l} \Big|_{\tilde{x}_t=-1}^{\tilde{x}_t=+1} ,
\end{aligned}
\tag{29}
$$

where Einstein's summation convention applies to the repeated indices k and p and the sums are evaluated at the coordinates

$$
\mathbf{y}(\tilde{x}_r, \tilde{x}_s, \tilde{x}_t) = \mathbf{y}^s + \frac{\tilde{x}_r}{2} L_1 \, \mathbf{e}'_1 + \frac{\tilde{x}_s}{2} L_2 \, \mathbf{e}'_2 + \frac{\tilde{x}_t}{2} L_3 \, \mathbf{e}'_3 \ . \tag{30}
$$

The $-1 < \tilde{x}_k < 1$ for $k = 1..N$ are the roots of the Legendre polynomial of degree N, which occur symmetrically about 0. For each expression, we take the difference between the sums evaluated at $\tilde{x}_k = 1$ and $\tilde{x}_k = -1$, corresponding to opposite faces of the cuboid.

For a tetrahedron, the displacement gradient can be obtained in a similar manner by integrating the equivalent surface tractions that concentrate along the four faces. The geometry of a tetrahedron is defined by the coordinates $\mathbf{y}^A$, $\mathbf{y}^B$, $\mathbf{y}^C$, and $\mathbf{y}^D$ of the four vertices A, B, C, and D. The faces ABC, BCD, CDA, and DAB are associated with the outward normal vectors $\mathbf{n}^D$, $\mathbf{n}^A$, $\mathbf{n}^B$, and $\mathbf{n}^C$, respectively. Using a Gauss-Legendre quadrature of degree N with the weights w_k and abscissas $\tilde{x}_k$ for $k = 1..N$, we obtain the approximation

$$
\begin{aligned}
u_{i,j}(\mathbf{x}) \approx & \frac{\mathcal{A}_{ABC}}{4} \sum_{r=1}^{N} \sum_{s=1}^{N} w_r w_s (1 - \tilde{x}_s) \, G_{ki,j}\left[\mathbf{x}; \mathbf{y}_{ABC}(\tilde{x}_r, \tilde{x}_s)\right] m_{kl} n_l^D \\
& + \frac{\mathcal{A}_{BCD}}{4} \sum_{r=1}^{N} \sum_{s=1}^{N} w_r w_s (1 - \tilde{x}_s) \, G_{ki,j}\left[\mathbf{x}; \mathbf{y}_{BCD}(\tilde{x}_r, \tilde{x}_s)\right] m_{kl} n_l^A \\
& + \frac{\mathcal{A}_{CDA}}{4} \sum_{r=1}^{N} \sum_{s=1}^{N} w_r w_s (1 - \tilde{x}_s) \, G_{ki,j}\left[\mathbf{x}; \mathbf{y}_{CDA}(\tilde{x}_r, \tilde{x}_s)\right] m_{kl} n_l^B \\
& + \frac{\mathcal{A}_{DAB}}{4} \sum_{r=1}^{N} \sum_{s=1}^{N} w_r w_s (1 - \tilde{x}_s) \, G_{ki,j}[\mathbf{x}; \mathbf{y}_{DAB}(\tilde{x}_r, \tilde{x}_s)] \, m_{kl} n_l^C \ ,
\end{aligned}
\tag{31}
$$

where $\mathcal{A}_{ABC}$ is the area of the triangular face ABC and we obtain the coordinates of summation with the mapping function

$$
\begin{aligned}
\mathbf{y}_{ABC}(\tilde{x}_r, \tilde{x}_s) = & \frac{1}{4} \mathbf{y}^A (1 - \tilde{x}_r)(1 - \tilde{x}_s) \\
& + \frac{1}{4} \mathbf{y}^B (1 + \tilde{x}_r)(1 - \tilde{x}_s) \\
& + \frac{1}{2} \mathbf{y}^C (1 + \tilde{x}_s) \ .
\end{aligned}
\tag{32}
$$

The coordinates $\mathbf{x}$ can be anywhere in the half-space, allowing the calculation of traction and stress along surface and volume elements, respectively.

We use the above numerical approach to build the stress interaction matrices used in Equation (27), considering the stress and traction caused by one volume element at a time, one component of plastic strain at a time. The calculation is performed once and the matrices are the same for every time steps. Illustrations of the distribution of abscissas and weights for integration along a rectangular or triangular face are shown in Figure 2a,b for Gauss-Legendre quadratures of order $N = 3$, $N = 7$, and $N = 15$, corresponding to increasing accuracy. We reduce the computational load while preserving numerical accuracy by

adapting the quadrature order based on distance from the source, using $N = 40$ in the near field, gradually lowering to $N = 3$ in the far field. We separate the Green's functions based on source and image and treat them with different quadrature orders, always using $N = 3$ for the image (see Appendix). We also distribute the computational load on different processors based on a distributed-memory architecture.

2.4 Representative stress in volume elements

As slip accumulates along a surface element or as plastic strain grows within a volume element, a complex spatial distribution of stress develops in the surrounding half-space. Within the deforming element and the surrounding ones, the stress field is heterogeneous and several strategies can be employed to select a representative value. With the collocation method, we select the central value of the element. This approach is commonly employed with the boundary integral method, and we adopt it for the surface elements. However, the collocation method is unstable for volume elements in a three-dimensional half-space [*Shi et al.*, 2022]. Therefore, we employ the Galerkin method, which consists in taking the average value within the element. Consider an arbitrary ambient stress field caused by local or remote plastic deformation, or even by distant fault activity. The average stress component within the element Ω is

$$\bar{\sigma}_{ij} = \frac{1}{V_\Omega} \iiint_\Omega \sigma_{ij}(\mathbf{y})\, \mathrm{d}\mathbf{y} \,, \tag{33}$$

where V_Ω is the volume of the element. We approximate Equation (33) using a Gauss-Legendre quadrature of order N. For a cuboid, the average stress can be approximated with

$$\bar{\sigma}_{ij} = \frac{1}{8} \sum_{r=1}^{N} \sum_{s=1}^{N} \sum_{t=1}^{N} w_r w_s w_t \, \sigma_{ij}[\mathbf{x}(\tilde{x}_r, \tilde{x}_s, \tilde{x}_t)] \,, \tag{34}$$

where the stress is evaluated at the coordinates

$$\mathbf{x}(\tilde{x}_r, \tilde{x}_s, \tilde{x}_t) = \mathbf{y}^s + \tilde{x}_r \frac{L_1}{2} \mathbf{e}'_1 + \tilde{x}_s \frac{L_2}{2} \mathbf{e}'_2 + \tilde{x}_t \frac{L_3}{2} \mathbf{e}'_3 \,. \tag{35}$$

Using $N = 1$, $\tilde{x}_1 = 0$, $w_1 = 2$, Equation (34) simplifies to the collocation method. For a tetrahedron, the average stress can be estimated with

$$\bar{\sigma}_{ij} = \frac{6}{64} \sum_{r=1}^{N} \sum_{s=1}^{N} \sum_{t=1}^{N} w_r w_s w_t (1 - \tilde{x}_r)(1 - \tilde{x}_t)^2 \sigma_{ij}[\mathbf{x}(\tilde{x}_r, \tilde{x}_s, \tilde{x}_t)] \,, \tag{36}$$

where the stress is evaluated at the coordinates

$$\begin{aligned} \mathbf{x}(\tilde{x}_r, \tilde{x}_s, \tilde{x}_t) = & \frac{1}{8}(1 - \tilde{x}_r)(1 - \tilde{x}_s)(1 - \tilde{x}_t)\, \mathbf{y}^A \\ & + \frac{1}{4}(1 + \tilde{x}_r)(1 - \tilde{x}_t)\, \mathbf{y}^B \\ & + \frac{1}{8}(1 - \tilde{x}_r)(1 + \tilde{x}_s)(1 - \tilde{x}_t)\, \mathbf{y}^C \\ & + \frac{1}{2}(1 + \tilde{x}_t)\, \mathbf{y}^D \,, \end{aligned} \tag{37}$$

where the $\tilde{x}_k$ and w_i are the abscissas and weights of the Gauss-Legrendre quadrature, respectively, and the geometry of cuboids and tetrahedra is defined in the previous section.

Illustrations of the distribution of abscissas and weights for volume integration within a cuboid or a tetrahedron with the Gauss-Legendre quadrature are shown in Figure 2b for orders $N = 3$, $N = 7$, and $N = 15$. To evaluate the representative stress with the Galerkin method, we use $N = 2$, leading to 8 integration points within the volume elements, providing fast, accurate, and numerically stable calculations.

2.5 Algorithm

The algorithm for the integral method involves the following steps. Starting from a mesh of surface and volume elements, we build the matrices of traction and stress interactions. We compute the stress caused by surface elements using analytic Green's functions suited for triangle [*Nikkhoo and Walter*, 2015] and rectangle [*Okada*, 1992] elements. For volume elements, we calculate the stress field numerically, integrating the Green's functions for a point source based on the geometry of cuboidal and tetrahedral elements. We evaluate the traction at the center of surface elements using the collocation method and the average stress within volume elements using the Galerkin method. The matrices are computed only once and used at every time step. Starting from an initial stress and possible state variables at time t, we simulate a time step using a Runge-Kutta method. We calculate the plastic strain-rate and fault slip-rate using the respective constitutive laws. We obtain the corresponding rates of stress and traction using matrix-vector operations. We conduct time integration to time $t + \Delta t$ with different orders of quadrature to obtain an estimate of numerical accuracy. Adaptive time steps result from using the largest step that satisfies a threshold accuracy. At time $t + \Delta t$, we obtain a new state of stress and traction, from which the procedure can be repeated. The method provides an apparatus to track the evolution of stress and traction where plastic deformation occurs. Complex simulations emerge from the nonlinear constitutive behavior of rocks, the coupling between brittle and ductile deformation, and geometrical effects. We simulate time series of geodetic data using separate matrices that connect slip and plastic strain to surface displacements. These calculations do not affect how the simulation proceeds. The code implementing these calculations compares successfully with other methods on the benchmark problems of the Sequence of Earthquakes and Aseismic Slip [*Erickson et al.*, 2020; *Jiang et al.*, 2022; *Erickson et al.*, 2023], but the viscoelastic effects remain untested.

3 Seismic cycles in a three-dimensional viscoelastic half-space

The integral method provides a procedure to keep track of evolving stress within the elastic half-space, to select representative values with surface and volume elements, and to simulate the accumulation of plastic strain, whether localized on faults or distributed in a viscoelastic domain. We illustrate the potential of the integral method with numerical simulations of seismic cycles in a three-dimensional viscoelastic half-space. Plastic deformation occurs by faulting in the brittle layer and viscoelastic flow in the underlying substrate. For the fault constitutive behavior, we assume that the frictional resistance is controlled by the real area of contact across the interface. The area of contact is an important property of fault zones that is directly affected by the effective normal stress and the size of micro-asperties around contact junctions, following [*Barbot*, 2019]

$$\mathcal{A} = \frac{c_0 + \mu_0 \bar{\sigma}}{\chi} \left(\frac{\theta V_0}{L} \right)^{\frac{b}{\mu_0}} , \tag{38}$$

where $\mathcal{A}$ is the real area of contact density, c_0 is the cohesion, μ_0 is a reference coefficient of friction, $\bar{\sigma}$ is the effective normal stress, and θ and L/V_0 are the age and characteristic lifetime of contact, respectively, with the characteristic weakening distance L and the reference velocity V_0. The dependence on the age of contact is weak, with a power-law exponent $b \ll 1$. The real area of contact controls the yield strength of the interface, as in

$$\sigma_Y = \mathcal{A} \chi , \tag{39}$$

where χ is the material hardness for plowing, i.e., the shear hardness. The fault slip-rate depends on the local shear stress relative to the yield strength, following a thermally activated power-law relationship [*Barbot*, 2019, 2022]

$$V = V_0 \left(\frac{\tau_s}{\sigma_Y} \right)^{\frac{\mu_0}{a}} \exp \left[-\frac{Q}{R} \left(\frac{1}{T} - \frac{1}{T_0} \right) \right] , \tag{40}$$

where V and V_0 are the instantaneous and a reference velocity, respectively, T is the local temperature, Q and T_0 are the energy and temperature of activation, respectively, with the universal gas constant R, and τ_s is the norm of the shear traction vector. The sensitivity to shear stress is exacerbated by the large power exponent resulting from $a \ll 1$. Shear stresses larger than the yield strength lead to high slip-rates. Reciprocally, shear stresses much lower than the yield strength lead to vanishing slip-rates. Under zero shear stress, the contact is stationary. Combining Equations (38), (39), and (40), we obtain the rate-, state-, and temperature-dependent friction law

$$V = V_0 \left(\frac{\tau_s}{c_0 + \mu_0 \bar{\sigma}} \right)^{\frac{\mu_0}{a}} \left(\frac{\theta V_0}{L} \right)^{-\frac{b}{a}} \exp\left[-\frac{Q}{R} \left(\frac{1}{T} - \frac{1}{T_0} \right) \right] , \tag{41}$$

where the material hardness χ has cancelled out. Equation (41) allows us to evaluate the instantaneous velocity based on the local shear stress, age of contact, and temperature. The evolutionary effects are captured by a thermally activated evolution law [*Barbot*, 2019]

$$\dot{\theta} = \exp\left[-\frac{H}{R} \left(\frac{1}{T} - \frac{1}{T_0} \right) \right] - \frac{V\theta}{L} , \tag{42}$$

where H and T_0 are the enthalpy and temperature of activation, respectively, of the healing mechanism [*Barbot*, 2022]. At steady-state, corresponding to $\dot{\theta} = 0$, we obtain a rate- and temperature-dependent shear traction, as follows

$$\tau_s = (c_0 + \mu_0 \bar{\sigma}) \left(\frac{V}{V_0} \right)^{\frac{a-b}{\mu_0}} \exp\left[\frac{aQ - bH}{\mu_0 R} \left(\frac{1}{T} - \frac{1}{T_0} \right) \right] . \tag{43}$$

The velocity dependence is controlled by $a - b$, with velocity-strengthening for $a - b > 0$, velocity-neutral for $a = b$, and velocity-weakening for $a - b < 0$. The mechanical behavior is temperature-hardening for $aQ - bH < 0$, temperature-neutral for $aQ = bH$, and temperature-softening for $aQ - bH > 0$. To fully describe fault slip, Equation (41) must be augmented to capture the orientation of the slip-rate vector. We assume that the slip-rate is parallel to the fault, such that $\mathbf{v} \cdot \mathbf{n} = 0$, and aligns with the local shear traction, as in $\mathbf{v} \times \mathbf{t}^s = \mathbf{0}$. In terms of components of the slip-rate vector, this can be written

$$v_i = V(\tau_s, \theta, T)\, \hat{t}_i^s , \tag{44}$$

where the shear traction $t_i^s = \tau_s \hat{t}_i^s$ is decomposed into the amplitude τ_s and the direction $\hat{t}_i^s$. Alternatively, the rake angle of the velocity vector in the fault plane is defined as

$$\alpha = \arctan \frac{t_2^s}{t_1^s} , \tag{45}$$

where t_1^s and t_2^s are the along-strike and up-dip components of the traction vector. A rake angle $\alpha = 0$ corresponds to left-lateral strike-slip faulting, and a rake $\alpha = 90°$ corresponds to thrust faulting if the fault dip angle is between 0 and 90°. Typically, the rake changes during rupture propagation [*Kirkpatrick and Brodsky*, 2014; *Kearse and Kaneko*, 2020]. Accordingly, we have the slip-rate components

$$\begin{aligned} v_1 &= V \cos\alpha \\ v_2 &= V \sin\alpha \\ v_3 &= 0 , \end{aligned} \tag{46}$$

where v_1, v_2, and v_3 are the strike-parallel, up-dip, and fault-normal components of the slip-rate vector, respectively.

The evolution of plastic strain in the Earth's lower crust and upper mantle is controlled by the rheology of rocks in high-temperature, high-pressure conditions. At steady-state, the stress versus strain-rate relationship is a thermally activated power-law with sensitivity to composition, grain size, water fugacity, and temperature [*Poirier*, 1985; *Hirth*

and Tullis, 1992; *Karato and Wu*, 1993; *Karato et al.*, 1986; *Rybacki and Dresen*, 2000; *Hirth and Kohlstedt*, 2003; *Karato and Jung*, 2003]. Upon perturbations, the steady-state behavior is preceded by a short-lived work-hardening phase called transient creep, characterized by a higher strain-rate [*Post*, 1977; *Peltier et al.*, 1980; *Ranalli*, 1980; *Chopra*, 1997; *Thieme et al.*, 2018]. Transient creep manifests itself measurably during the postseismic phase of the seismic cycle [*Freed et al.*, 2010; *Masuti et al.*, 2016; *Tang et al.*, 2019, 2020]. We adopt a constitutive behavior that captures the transient and steady-state response compatible with laboratory observations [*Masuti et al.*, 2016; *Masuti and Barbot*, 2021]. For a representative volume element, the constitutive law can be described by a nonlinear Burgers assembly of springs and dashpots placed in series in a Maxwell element and in parallel in a Kelvin element. The total plastic strain-rate is decomposed into

$$\dot{\epsilon}^p_{ij} = \dot{\epsilon}^M_{ij} + \dot{\epsilon}^K_{ij} \ , \tag{47}$$

where $\dot{\epsilon}^M_{ij}$ and $\dot{\epsilon}^K_{ij}$ are the plastic strain-rates in the Maxwell and Kelvin elements, respectively. The plastic strain-rate in the Maxwell element represents steady-state creep and obeys the following constitutive law

$$\dot{\epsilon}^M_{ij} = A_M \, \tau^{n_M - 1} \sigma'_{ij} \ , \tag{48}$$

where σ'_{ij} is the deviatoric stress tensor defined in Equation (3), the prefactor A_M contains the effects of composition, grain size, water fugacity, and temperature, considered spatially variable, but constant throughout the simulation, and n_M is the power-law exponent. The formulation captures various creep mechanisms depending on the constitutive parameters. Diffusion creep, grain-boundary sliding, and dislocation creep assume $n_M = 1$, $n_M = 2$ and $n_M = 2 - 5$, respectively, with different prefactors. The plastic strain-rate in the Kelvin element is controlled by the effective stress

$$Q_{ij} = \sigma'_{ij} - 2\mu_K \, \epsilon^K_{ij} \ , \tag{49}$$

where μ_K is the work-hardening coefficient and the term $2\mu_K \, \epsilon^K_{ij}$ represents the internal stress due to the activation of sub-optimally oriented slip systems [*Masuti and Barbot*, 2021]. The effective stress is always deviatoric and can be further characterized by its norm

$$q = \left(Q_{ij} Q_{ij} \right)^{1/2} \ , \tag{50}$$

where Einstein's summation convention is implied. The resulting plastic strain-rate in the Kelvin element obeys the following constitutive relationship

$$\dot{\epsilon}^K_{ij} = A_K q^{n_K - 1} Q_{ij} \ , \tag{51}$$

where the coefficient A_K contains the effects of composition, grain-size, and temperature, and n_K is the power-law exponent. The Kelvin strain ϵ^K_{ij} can be considered a state variable for distributed viscoelastic deformation, capturing the effect of internal stress within a representative volume element. As the Kelvin strain accrues, the effective stress reduces, leading to a work-hardening response. Asymptotically, the Kelvin strain-rate vanishes, and the deformation continues with strain accumulation in the Maxwell element, embodying the steady-state behavior. Much experimental data are available to describe the steady-state parameters [e.g., *Karato et al.*, 1986; *Kirby and Kronenberg*, 1987; *Koch et al.*, 1989; *Shea and Kronenberg*, 1992; *Evans and Kohlstedt*, 1995; *Dimanov and Dresen*, 2005; *Hansen et al.*, 2011; *Tokle et al.*, 2019]. In practice, the constitutive parameters A_M and A_K and n_M and n_K, respectively, are of similar orders of magnitude and the work-hardening coefficient μ_K is of the order of the local shear modulus. Experimental data on dry and wet dunites, which are relevant for mantle flow, indicate a nonlinear stress versus strain-rate relationship for the work-hardening phase [*Masuti and Barbot*, 2021].

The constitutive assumptions described here allow us to predict fault slip-rate and distributed plastic strain-rate given the current stress and the relevant state variables. Consideration of these relationships with the conservation of momentum forms a closed system of equations that can be solved with the integral method and numerical time stepping.

Next, we illustrate the method with examples for strike-slip and thrust faulting in a three-dimensional viscoelastic half-space.

3.1 Strike-slip faulting over a viscoelastic lower crust

We consider three-dimensional models of seismic cycles in a viscoelastic half-space with a vertical strike-slip fault overlying a viscoelastic lower crust (Figure 3). The elastic parameters are for a Poisson's solid with $\lambda = \mu = 30\,\text{GPa}$. The fault is 60 km long, extending from the surface to 20 km depth, and undergoes a long-term right-lateral slip-rate of 30 mm/yr. Spontaneous earthquake nucleation is favored by a 30 km-long steady-state velocity-weakening region extending from the surface to 15 km depth (Figure 3a). The distribution of frictional parameters and effective normal stress is taken from the Sequence of Earthquake and Aseismic Slip benchmark problem BP-4 [*Jiang et al.*, 2022], except for the fault dimension. Notably, we have $a - b = 0.012$ in the velocity-strengthening region and $a - b = -0.0065$ in the velocity-weakening region. With a characteristic weakening distance $L = 5\,\text{cm}$ and an effective normal stress $\bar{\sigma} = 50\,\text{MPa}$, we obtain a characteristic nucleation size of 4.6 km and a concentration of the rupture front over a cohesion zone of 2.3 km. This is well resolved by a mesh of square elements with a uniform sampling size of 1 km, resulting in 1,200 surface elements.

The ductile lower crust extends from 20 to 40 km depth and is sampled by a $60 \times 60 \times 20\,\text{km}$ mesh of $5 \times 5 \times 5\,\text{km}$ cubic elements centered on the fault, resulting in 576 volume elements (Figure 3b). The distribution of viscosity follows a mylonite shear zone extending below the fault in the lower crust. Viscoelastic flow operates at steady-state with the lowest viscosity of $\eta = 10^{18}\,\text{Pa s}$, corresponding to $A_M = 10^{-12}\,/(\text{MPa s})$, increasing gradually to a background value of $5 \times 10^{19}\,\text{Pa s}$ away from the fault. The shear zone deforms with a long-term strain-rate of $\dot{\epsilon}^L_{12} = 2 \times 10^{-15}/\text{s}$.

We simulate seismic cycles for a period of 400 years. The simulation produces four earthquakes that nucleate near the surface and propagate bilaterally as crack-like ruptures (Figure 4). The interseismic period is characterized by a long period of quiescence with a locked seismogenic zone followed in a later stage by rapid inward progression of creep into the velocity-weakening region. The development of creep waves culminates with the nucleation of seismic ruptures. Each seismic event triggers a postseismic relaxation phase with accelerated creep around the rupture, the so-called afterslip. The coseismic stress perturbation triggers viscoelastic relaxation in the lower crust characterized by a rapid flow during a transient phase. The accelerated creep returns to the background strain-rate or below within 15 years of the mainshock.

The coupling between fault dynamics and lower-crustal flow is further illustrated in Figure 5. Rupture nucleation occurs at the center of the velocity-weakening region, near the free surface. At a critical slip-rate, nucleation transitions to outward rupture propagation at slip-rates approaching 1 m/s. The rupture propagates radially until it saturates the seismogenic zone. As the rupture stops due to the velocity-strengthening behavior of the surrounding region the velocity-weakening region rapidly relocks and rapid afterslip concentrates around the boundaries of the rupture. After 5 years, afterslip is mostly dissipated, the fault creeps, and the seismogenic zone is locked. During the early phase of the postseismic period, high plastic strain-rate concentrates in the lower crust concentrating below the fault ruptured area. Viscoelastic flow is fastest below the fault zone, attaining rates of $10^{-12}/\text{s}$, which is a thousand times faster than the background strain-rate. As the coseismic stress change dissipates during viscoelastic relaxation, the flow decelerates. After 25 years, the distribution of plastic strain-rate is more uniform, with some regions flowing more slowly than the long-term strain-rate.

Crustal dynamics induces surface deformation with specific patterns of horizontal displacement, uplift, and subsidence that are characteristic of the deformation mechanisms. Numerical simulations with the integral method allows us to evaluate surface displace-

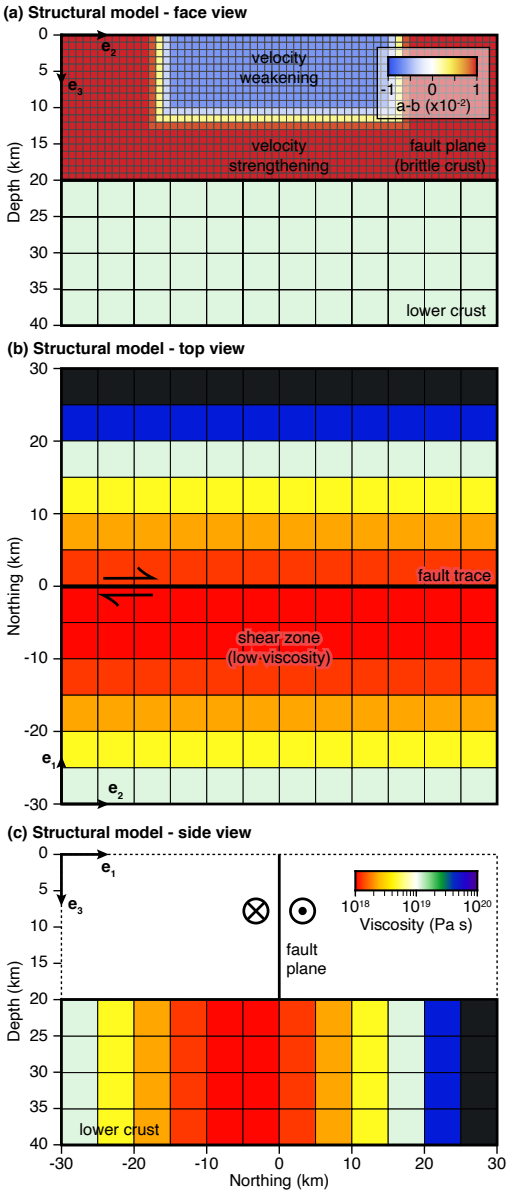

Figure 3: Structural model for seismic cycles on a right-lateral strike-slip fault overlying a viscoelastic lower crust in a half space. a) Face view showing the extent of the fault from the surface to 20 km depth with a 30 km-long velocity-weakening section. The distribution of the steady-state velocity dependence parameter $a - b$ is tapered. The frictional parameters are taken from the Sequence of Earthquake and Aseismic Slip benchmark problem BP4 [*Jiang et al.*, 2022]. The bottom layer shows the viscosity and rectilinear mesh of the lower crust. b) Top view showing the fault trace and the spatial distribution of viscosity in the lower crust in map view. The viscosity corresponds to a mylonite shear zone below the fault. c) Side view showing the distribution of viscosity in side view. The distribution of viscosity is chosen to illustrate lateral variations of rheological properties.

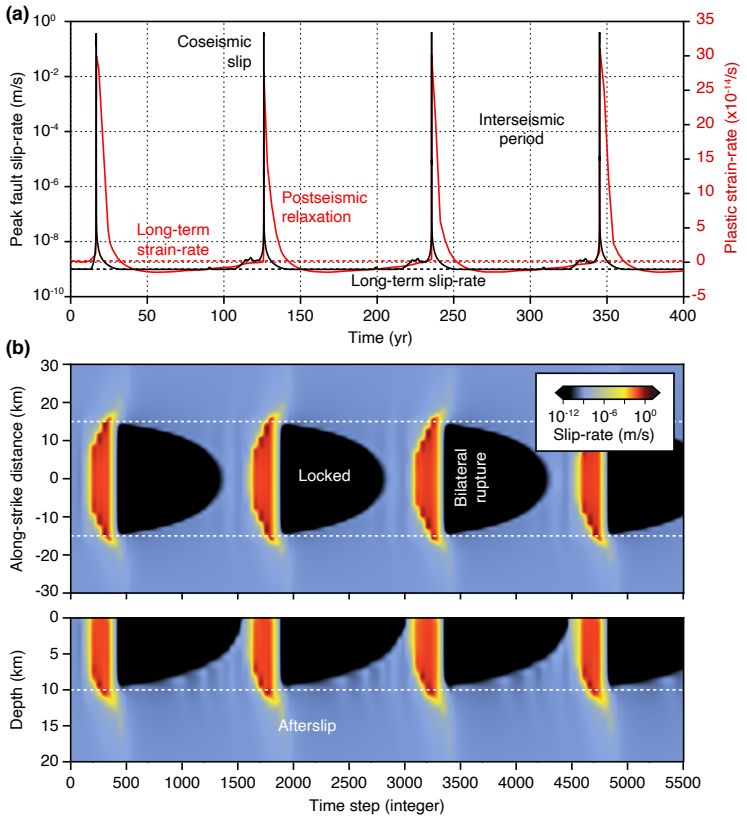

Figure 4: Numerical simulation of seismic cycles on a strike-slip fault overlying a viscoelastic lower crust. a) Time series of peak velocity (black line) and plastic strain-rate below the center of the fault (red line) for a period of 400 years showing four seismic events followed by viscoelastic relaxation. Peak slip-rate is 0.4 m/s. The dashed lines indicate the long-term rates. Viscoelastic flow commonly exceeds the background loading-rate during the postseismic period and proceeds at smaller rates during the interseismic period. b) Evolution of fault slip during seismic cycles in horizontal and vertical profiles. The horizontal profile extends 60 km along the fault at 5 km depth. The vertical profile extends from the surface to 20 km depth at the center of the fault. The x-axis is computational time steps, which are adaptive from 50 ms to 0.1 year. Nucleation occurs by long-term creep waves propagating inward into the velocity-weakening region. The ruptures represent bilateral crack-like propagation.

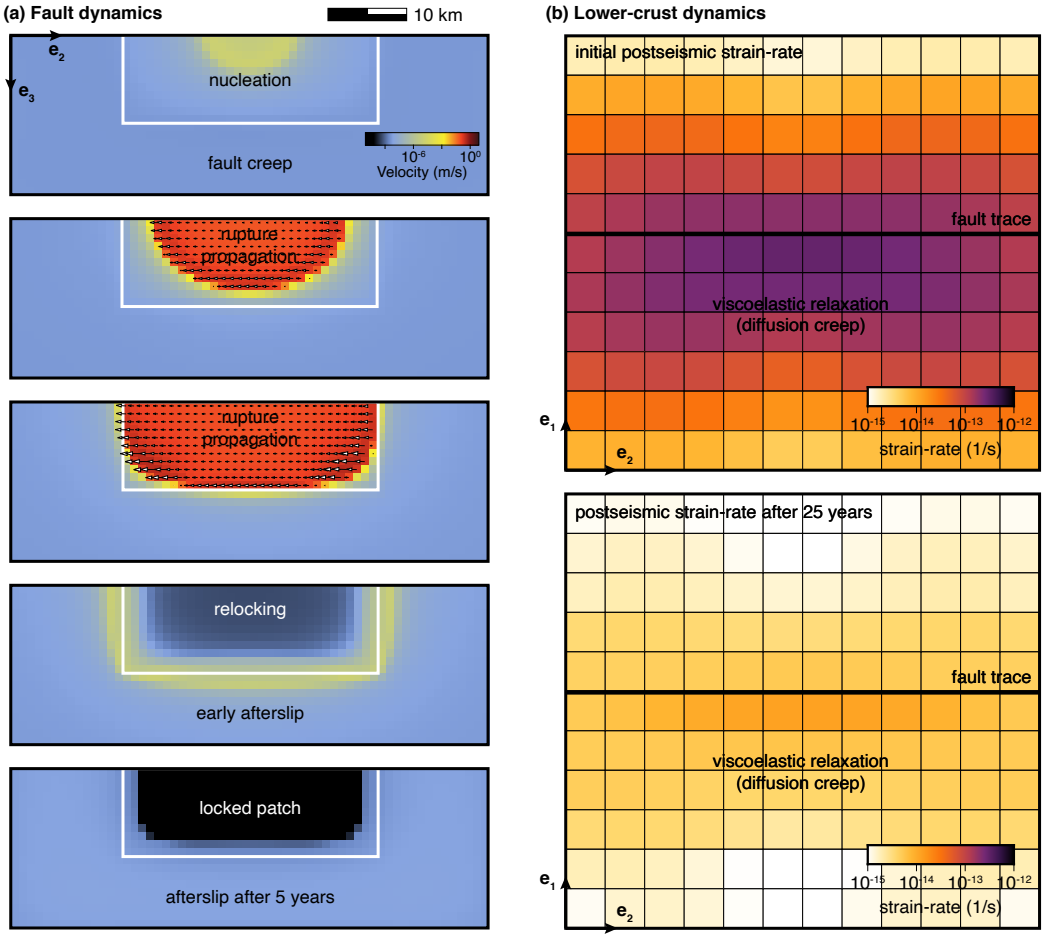

Figure 5: Evolution of fault slip and lower-crustal viscoelastic flow during and following a seismic event. a) Evolution of fault slip along the fault plane with rupture nucleation, propagation, termination, and relocking, followed by afterslip. The background color indicates the local slip rate. The arrows indicate the direction of slip toward the observer, compatible with right-lateral slip. b) Distribution of plastic strain-rate in map view, showing the top of the lower crust. The fault trace is shown for reference. The squares indicate the rectilinear mesh of cuboid elements. The length scale is the same for all plots.

ments at arbitrary distances from the source of deformation and to separate the components of surface displacements attributed to fault slip or viscoelastic flow. This is made possible because the displacement field can be obtained anywhere in the half-space using distinct Green's functions for surface and volume elements. Figure 11 shows the surface deformation after the first simulated earthquake at a late stage of the postseismic period. The deformation caused by faulting is characterized by a four quadrants of uplift and subsidence in the near-field close to the rupture tip associated with compressional and extensional stress. Horizontal displacements are characteristic of a right-lateral dislocation with fault-parallel displacements along the fault and rotation of the vector field in the fault-perpendicular direction near the rupture tip. The deformation may be characterized by two counter-clockwise rotations in the far field. In the far-field, there are additional four quadrants of uplift and subsidence in opposite direction to the near field.

The deformation induced by viscoelastic flow in the lower crust is far more distributed and of overall lower amplitude due to the greater confinement depth of the source (Figure 11b). The pattern of uplift and subsidence is opposite to the one caused by fault slip, compatible with a viscoelastic rebound of the Earth's surface during the postseismic period. The pattern of horizontal motion is compatible with a double-couple, with a larger amplitude of displacement away from the fault. The vertical displacements are caused by the relaxation of vertical shear stress in the lower crust. The surface displacements are the sum of the ones caused by fault slip and viscoelastic flow. The time series of surface displacement reveal a dominant east-west cumulative displacement with successive earthquake cycles (Figure 11c). The simulated time series resemble typical geodetic time series of tectonic deformation that can be decomposed into the coseismic, postseismic, and interseismic phases of the seismic cycle. The linear trends in each displacement component result from the long-term deformation of the fault and the underlying lower crust, that accumulate permanent strain. The sudden coseismic displacements occur due to seismic events that last just a few seconds. The following postseismic transient is the result of afterslip and viscoelastic relaxation. The contribution of viscoelastic flow represents about 10% of that of fault slip. In the far field, fault slip and viscoelastic flow produce opposite trends of vertical displacement. Such distinct spatial patterns and time scales of postseismic displacements from afterslip, relocking of the seismogenic zone, and viscoelastic relaxation can in principle be used to constrain the mechanical properties of the lithosphere.

We now extend the model to take into account more structural complexity. We consider strike-slip faulting in a tectonic setting where the lithosphere is thinned and the Mohorovičić discontinuity (Moho) is deflected upward. We assume that the ductile lower crust is advected along at constant thickness. To capture the non-planar geometry, we build a curvilinear mesh of the lower crust using tetrahedral volume elements (Figure 7). We use a Gaussian function to model the 5 km deflection of the lower crust. Conceptually, the mesh is formed by $12 \times 12 \times 3$ parallepiped elements of dimension $5 \times 5 \times 5$ km. In practice, each parallepiped is meshed with 6 tetrahedra connecting 4 different vertices, resulting in 2,592 tetrahedral volume elements. The shear zone deforms with a long-term strain-rate of 10^{-15}/s with lateral variations of viscosity as low as $\eta = 10^{18}$ Pa s at the center of the shear zone, gradually increasing to $\eta = 10^{18}$ Pa s some 30 km away (Figure 7a).

The 400-year simulation produces four seismic events with slightly shorter recurrence times than in the previous example due to the curved geometry of the lower crust and the different long-term strain-rate. The seismic ruptures nucleate at the center of the seismogenic zone near the free surface after a long inward migration of creep inside the velocity-weakening domain. The nucleation then transitions to outward rupture propagation. When the rupture stops, we enter the postseismic phase of the seismic cycle with concentration of afterslip around the rupture and the onset of viscoelastic relaxation in the lower crust. After relocking of the seismogenic zone, afterslip continues for several years diffusing outward and toward greater depths. After 6 years of viscoelastic relaxation, the

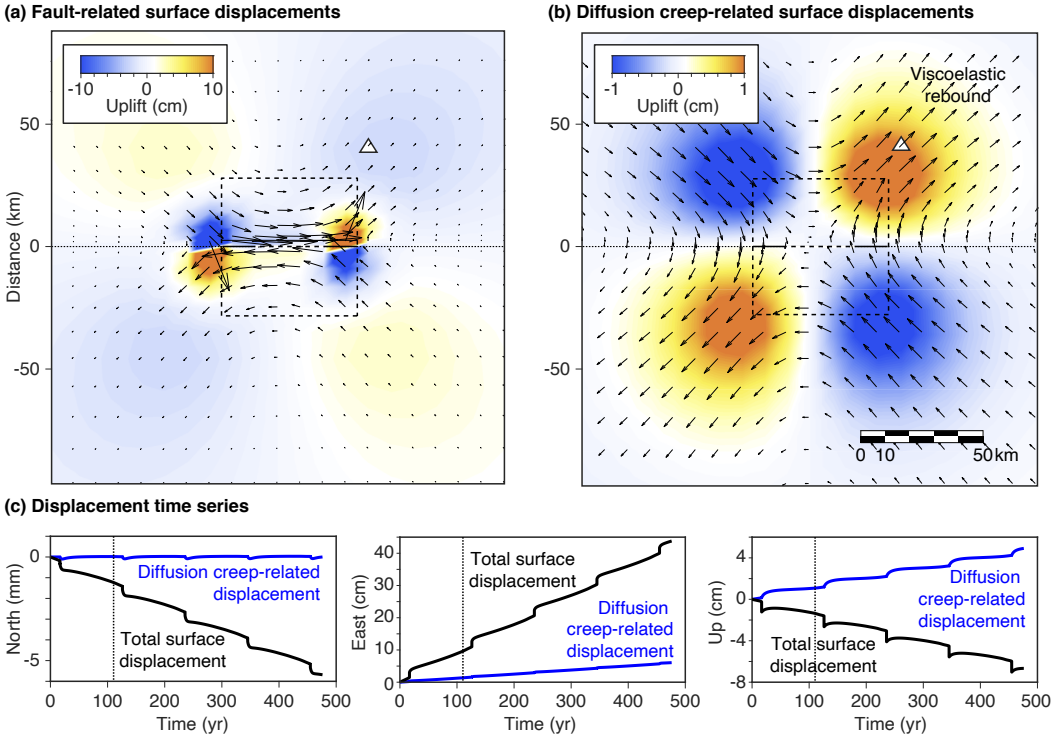

Figure 6: Crustal deformation during seismic cycles in a viscoelastic half-space. a) Surface deformation induced exclusively by fault slip. The arrows indicate cumulative horizontal displacements. The background color indicates uplift and subsidence. The triangle indicates the location of a geodetic station with time series shown in c). The displacement is anti-symmetric with respect to the north axis. The extent of the velocity-strengthening and velocity-weakening fault sections are shown in solid and dashed segments, respectively, for reference. The extent of the rectilinear mesh for the lower crust is shown with the dashed box. The contribution of viscoelastic flow represents 10% of long-term displacements in the east direction. The use of Green's functions with the integral method allows the calculation of surface displacement at arbitrary distances from the mesh. b) Surface displacements induced exclusively by viscoelastic flow, showing four quadrants of uplift and subsidence in the far field. c) Displacement time series at the geodetic station in a) and b). The displacement is decomposed into the total deformation (black) and the contribution of viscoelastic flow (blue).

plastic strain still accumulates rapidly below the fault due to quasi-static stress transfer by afterslip.

The examples demonstrate successful simulations of seismic cycles in a viscoelastic half-space using cuboidal and tetrahedral volume elements based on a linear viscoelastic rheology with lateral variation of rheological properties for earthquakes on a strike-slip fault. In the next section, we discuss other cases that illustrate the model for a thrust fault with linear and nonlinear rheology in the lower crust.

3.2 Thrust fault overlying a deflected Mohorovičić discontinuity

We now consider other applications of the integral method for a more structurally complex tectonic setting with a thrust fault overlying a lower crust deflected by the flexure of the Moho (Figure 8). We will compare results with a linear and nonlinear rheology in the lower crust. The fault is 60 km long, 40 km wide, dipping 30.5° to the south. The fault is characterized by a central velocity-weakening region extending from the surface to approximately 22 km in the down-dip direction, corresponding to a depth of 15 km. The effective normal stress $\bar{\sigma} = 50$ MPa and the characteristic weakening distance $L = 5$ cm are uniform, but the steady-state velocity-dependence parameter varies spatially with $a - b = 0.012$ in the velocity-strengthening region and $a - b = -0.0065$ in the velocity-weakening region. We discretize the fault with 60 and 40 square patches in the along-strike and down-dip directions, respectively, resulting in 2,400 surface elements (Figure 8a).

The viscoelastic substrate in the lower crust is bulged over a distance of approximately 50 km with a uniform thickness of 15 km. The Moho depth varies between 30 and 35 km. We mesh the viscoelastic domain with 3456 tetrahedral elements (Figure 8a). In this first example, the lower crust follows a Maxwell rheology with a uniform viscosity of 10^{18} Pa s. The lower-crust is placed in a tectonic regime of horizontal shortening and vertical thickening. Accordingly, we choose a background strain-rate with $\dot{\epsilon}^L_{11} = -10^{-15}$ s and $\dot{\epsilon}_{33} = 10^{-15}$ s, all other terms being identically zero.

We simulate the seismic cycle for a period of 400 years, producing 3 large ruptures that break the entire seismogenic zone with 5 m of coseismic slip. The rupture proceeds in a similar manner with nucleation on the side of the velocity-weakening region near the free surface (Figure 8b). The rupture then fills up the seismogenic zone and propagates unilaterally toward the other side of the fault. This is followed by a postseismic phase with concentration of afterslip around the coseismic rupture, relocking of the seismogenic zone, and the diffusion of afterslip across the fault plane in the following years. The nucleation of earthquakes often follows a sequence of slow-slip events that propagate at the bottom of the seismogenic zone while creep penetrates inside the velocity-weakening domain. As a result, at the end of the interseismic period, the locked zone is much smaller than the velocity-weakening region.

The postseismic phase is characterized by rapid strain-rate in the lower crust, concentrating in the region immediately below the seismogenic zone (Figure 10). The distribution of plastic strain-rate is stationary for a few days, consistent with the characteristic relaxation time of 1 year for a viscosity of 10^{18} Pa s and a rock rigidity of 30 GPa. After 6 years, plastic strain accumulation migrates toward the bottom of the thrust fault, driven by the relaxation of initial stress below the seismogenic zone and the quasi-static stress transfer by afterslip toward the deep velocity-strengthening region of the fault farther south. After 16 years, the plastic strain-rate returns to its background value, except for the lasting effect of afterslip that causes a plastic strain accumulation at the intersection with the thrust fault. The simulation illustrates the effect of mechanical coupling between afterslip and viscoelastic flow during the seismic cycle, leading to a non-stationary distribution of deformation in the lower crust.

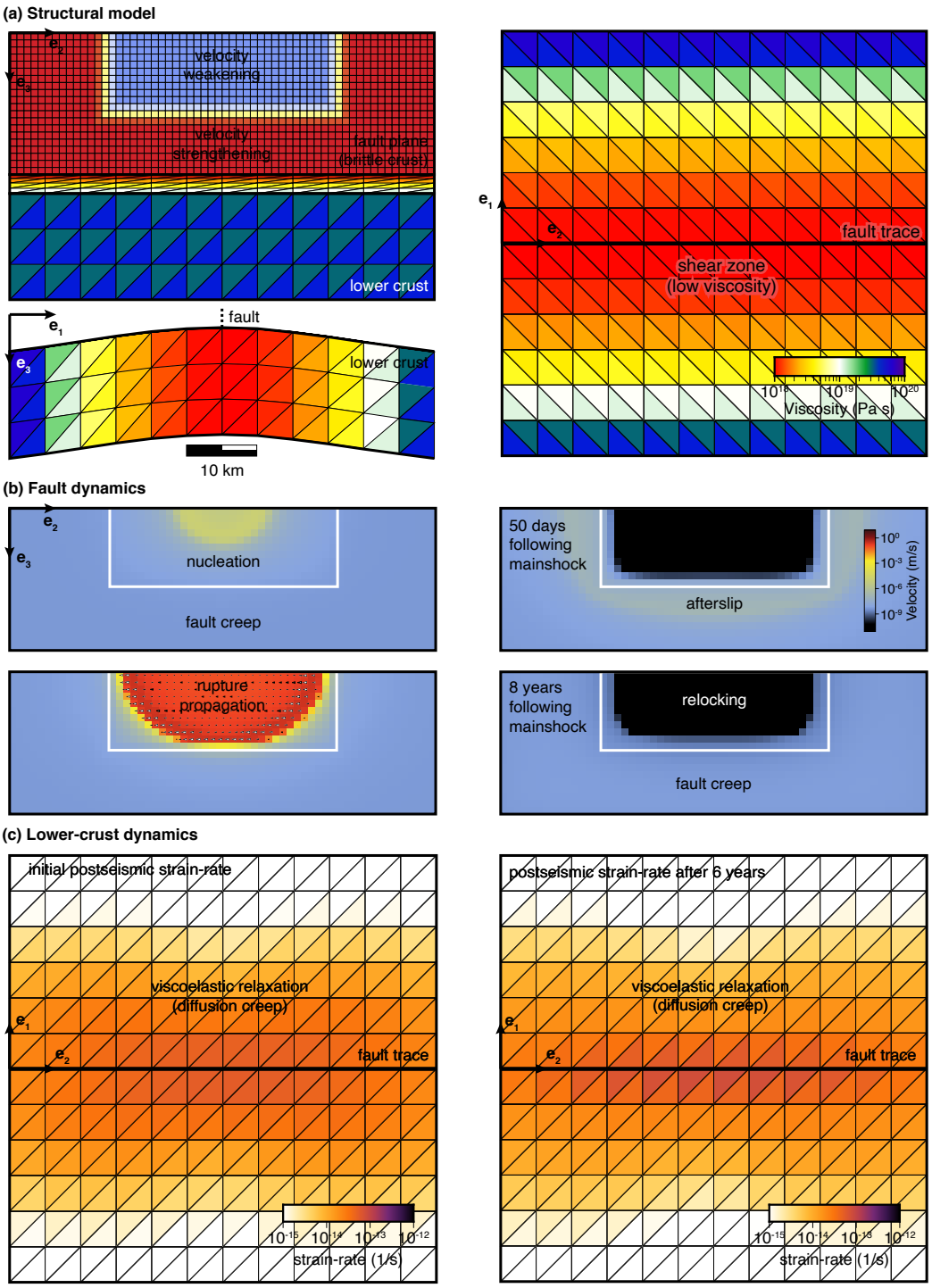

Figure 7: Simulation of seismic cycles in a viscoelastic half-space with a curvilinear mesh of tetrahedral elements in the ductile lower crust. a) Structural model shown in face, side, and top views. The fault geometry and distribution of frictional properties is similar as in Figure 3. The lower crust follows the flexure of the Moho with a constant thickness. The distribution of viscosity is centered about the fault trace, corresponding to a mylonite shear zone. b) Evolution of fault slip during a single seismic cycle. The color scale and arrows indicates the amplitude and orientation of slip-rate. The plots illustrate rupture nucleation and propagation, the onset of early afterslip, and relocking of the seismogenic zone. c) Distribution of plastic strain-rate at the top of the lower crust immediately after the earthquake, and 6 years later. Viscoelastic flow concentrates below the fault trace at a later stage of postseismic relaxation because of reloading by afterslip. The triangles indicate the top of the tetrahedra forming the curvilinear mesh. The plastic strain-rate is uniform within each volume element.

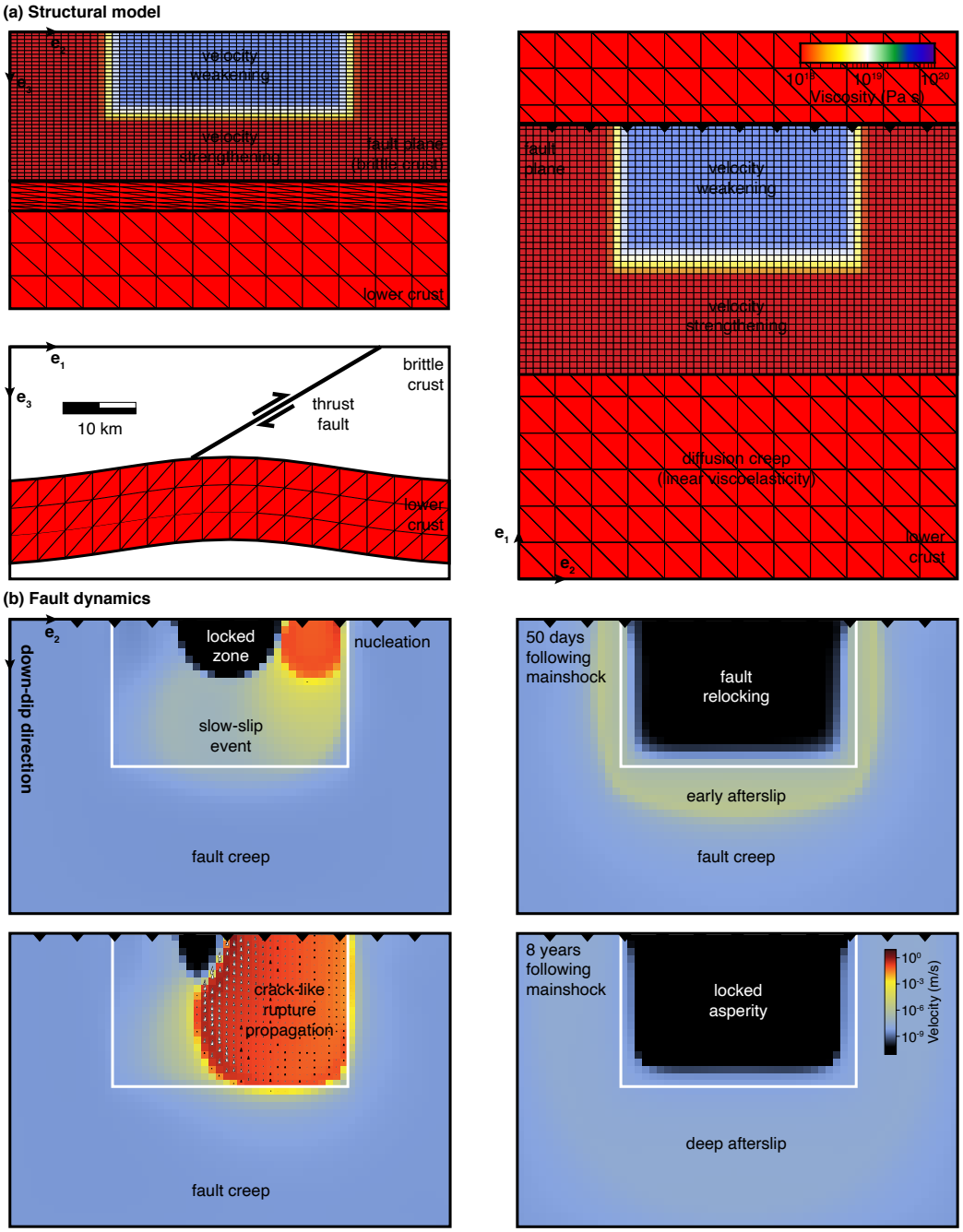

Figure 8: Simulation of seismic cycles on a thrust fault overlying a viscoelastic lower crust in a half space. a) Structural model with a 30°-dipping thrust fault extending from the surface to 20 km depth. The color on the fault indicates the distribution of the steady-state frictional parameter $a - b$, as in Figure 5. The lower crust follows the flexure of the Moho with a constant thickness of 15 km. The lower crust discretized in a curvilinear mesh of tetrahedral elements with a uniform viscosity. b) Evolution of fault slip during a single seismic cycle, with nucleation of the side of the fault next to a locked zone, unilateral rupture propagation and rapid relocking. Every seismic event is succeeded by afterslip starting in the periphery of the rupture, diffusing outward inside the velocity-strengthening region.

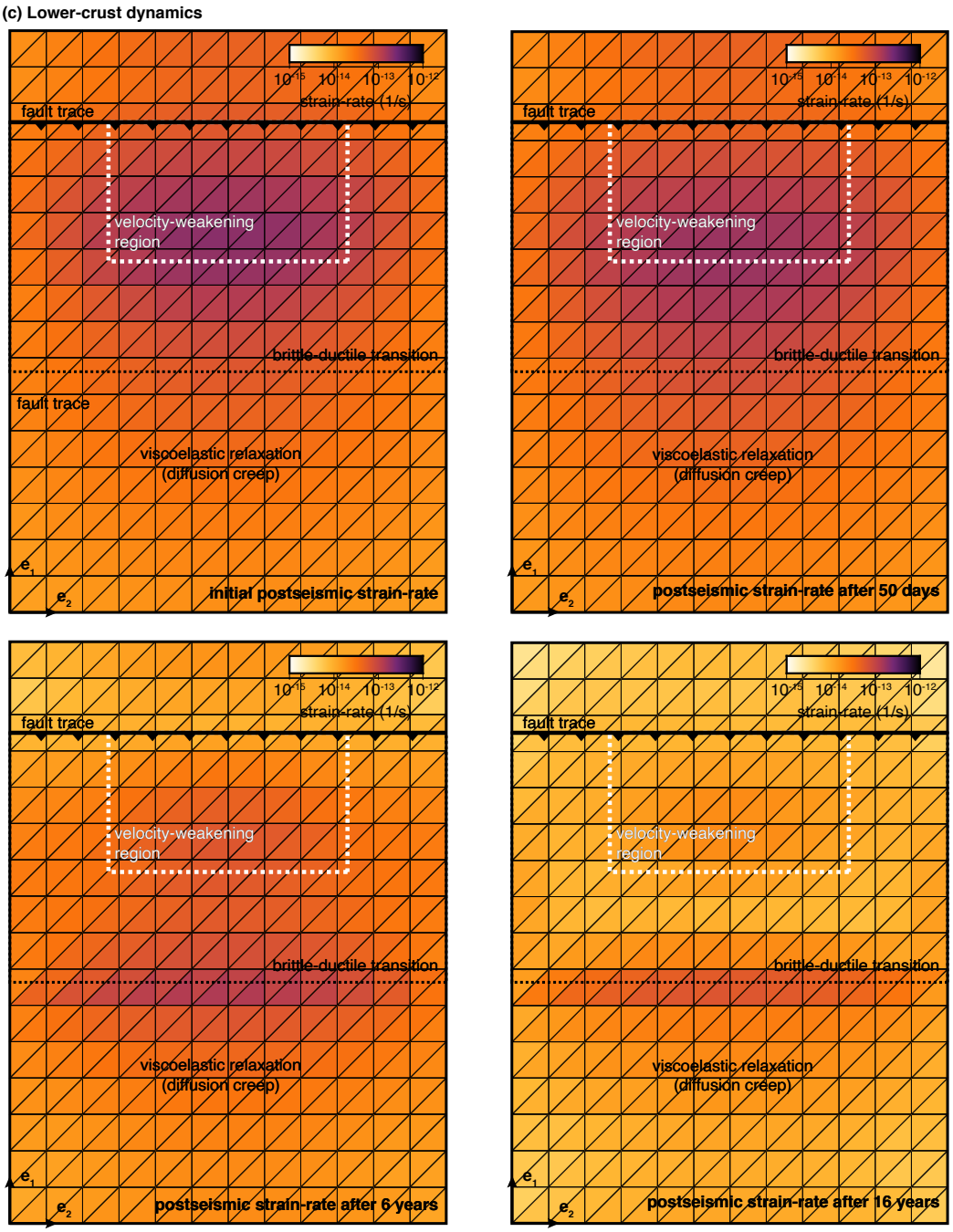

Figure 9: c) Evolution of plastic strain-rate in the lower crust during the postseismic phase of the seismic cycles for a thrust fault. The snapshots show the distribution of plastic strain-rate in map view (background color) immediately after the mainshock and 50 days, 6 years, and 16 years into the postseismic period. The thick black line with chevrons indicate the fault trace. The dashed white box indicates the surface projection of the velocity-weakening region that confines the coseismic rupture. The horizontal black dashed line indicates the intersection between the fault and the lower crust. The plastic strain initially concentrates near the bottom of the seismogenic zone, which produces high coseismic slip and is closer to the lower crust, leading to a higher stress change. After 16 years, plastic strain accumulates near the bottom of the thrust fault, due to reloading by afterslip.

We evaluate the surface displacement caused by crustal dynamics in the middle of the postseismic phase. We decompose surface displacements into the contributions of fault slip and distributed plastic strain (Figure 10). Fault slip creates latitudinal shortening and uplift above the thrust, as expected (Figure 10a). The effect of viscoelastic relaxation in the postseismic period is also latitudinal shortening, but this is accompanied by longitudinal extension and a distinct pattern of uplift and subsidence (Figure 10b). Postseismic subsidence concentrates above the thrust and uplift extends to the south, both contributing to a viscoelastic rebound of the Earth's surface. Furthermore, the viscoelastic longitudinal shortening centers in the middle of the fault, creating retrograde motion in the horizontal direction.

Time series of surface displacement reveal the contribution of fault slip and viscoelastic flow (Figure 10c). Viscoelastic effects are relatively small in the horizontal direction. However, afterslip and viscoelastic relaxation have similar amplitude and sense of motion in the postseismic period for the vertical displacement. In principle, measurements of surface displacements may differentiate these effects provided sufficient geodetic coverage in time and space. Notably, viscoelastic effects continue to produce surface displacements for at least a hundred years.

We now consider the effect of a nonlinear rheology in the lower crust. We consider a wet quartz rheology [*Rutter and Brodie*, 2004] operating at 900°C with an activation energy of 242 kJ/mol and power exponent $n_M = 3$ resulting in a lumped parameter $A_M = 5.0 \times 10^{-11}$ MPa^{-n}/s. The rheological parameters are uniform. We simulate seismic cycles on the thrust fault with the same frictional constitutive parameters for a period of 400 years. The sequence features similar characteristics as for the linear rheology, but the recurrence time of earthquakes is slightly affected, occurring about 1-1.5 years sooner than with a Maxwelian lower crust. The deformation of the lower crust during the postseismic period is localized to high coseismic stress regions (Figure 10). The deformation is stationary for a few days after the mainshock, but eventually migrates south after 5 years of postseismic relaxation. After 15 years, the deformation of the lower crust localizes at the intersection with the thrust fault, similar to, but in a more pronounced way than with a linear rheology.

The surface displacements in the postseismic period are shown in Figure 11. The surface displacements caused by viscoelastic relaxation of a power-law rheology has a similar spatial pattern as with the linear rheology, with retrograde horizontal motion and viscoelastic rebound in the vertical direction, but the vertical displacements are more subdued. This is caused by the smaller deforming volume of the lower crust, as the plastic strain accumulation concentrates in regions of high coseismic stress. Overall, the deformation of the lower crust with the nonlinear rheology considered is slower than in the linear case by a factor of two.

These examples illustrate some key capabilities of the integral method, such as the integration of nonlinear frictional and rheological constitutive laws, lateral variations of constitutive parameters, and curvilinear domains. The method captures the dynamics of the lithosphere during all phases of the seismic cycle for strike-slip, thrust, and normal faults, and resolves time series of crustal deformation at arbitrary distances from the source, documenting separately the contributions of fault-related processes and viscoelastic flow. In the next section, we illustrate applications in a two-dimensional viscoelastic half-space.

4 Seismic cycles in a two-dimensional viscoelastic half-space

Finally, we illustrate applications of the integral method for a two-dimensional viscoelastic half-space within the in-plane strain approximation. Other useful applications in anti-plane strain are readily implemented and tested. However, they are typically less numerically intensive or structurally complex than for in-plane strain, so we do not present

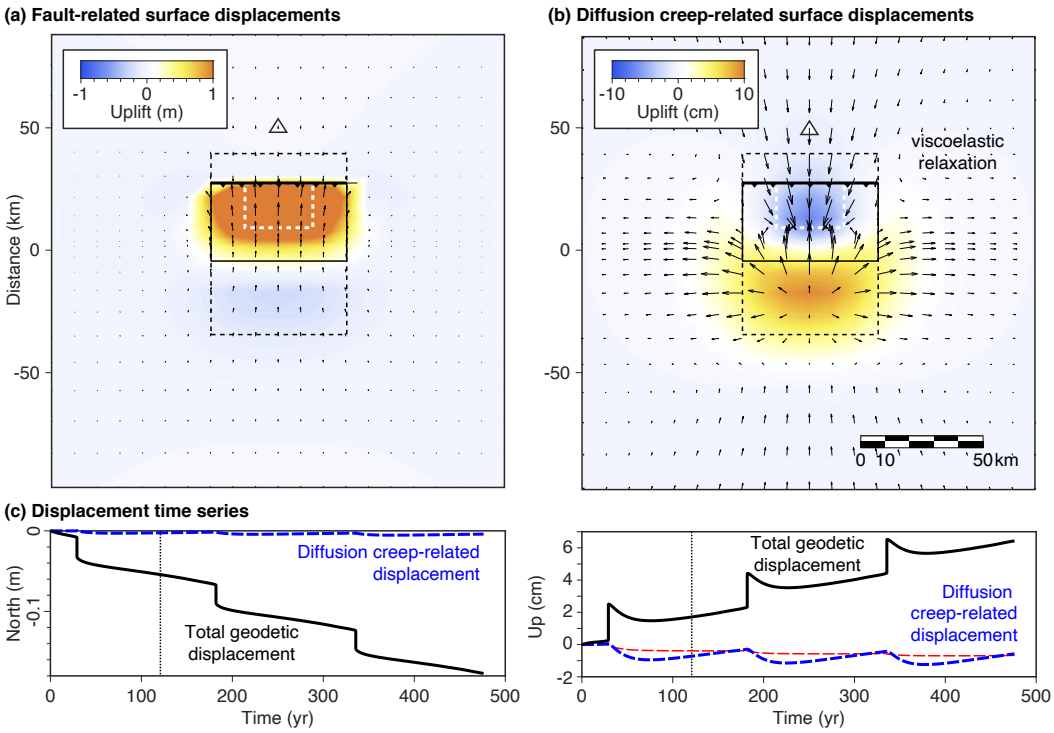

Figure 10: Crustal deformation during seismic cycles on a thrust fault overlying a viscoelastic lower crust. a) Surface displacement caused exclusively by fault slip. b) Surface displacements caused by viscoelastic flow. The shortening occurs farther south leading to retrograde postseismic motion with a vertical rebound. The horizontal and vertical displacements are shown with arrows and background color, respectively, showing shortening across the fault trace and uplift above the thrust fault. The thick black line with chevrons indicates the fault trace. The surface projection of the fault is shown with the solid black box. The extent of the seismogenic zone is shown with the white dashed box. The footprint of the curvilinear mesh of the lower crust is shown in dashed black rectangle. c) Cumulative displacement time series during the seismic cycle for the geodetic station shown with a triangle in a) and b) for north and vertical components. The east component is identically zero for this station. The total displacement is shown in black and the contribution of viscoelastic flow by diffusion creep in blue. The shortening is mostly contributed by faulting. However, viscoelastic effect dominate the surface deformation during the postseismic phase in the vertical direction. The results for dislocation creep in Figure 10 are shown in the thin red line, for comparison.

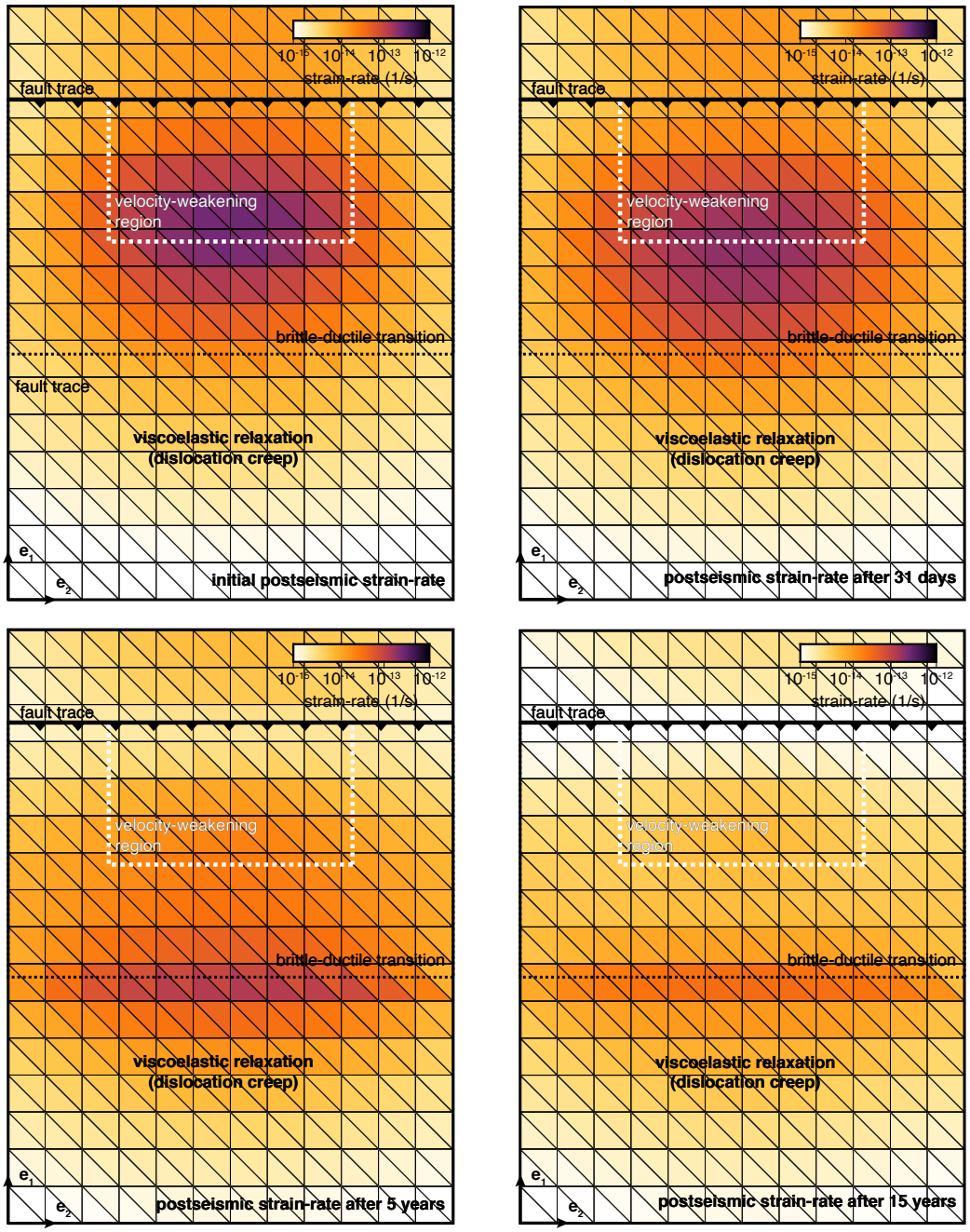

Figure 11: Viscoelastic relaxation in the lower crust with power-law flow. The postseismic transient is caused by a coseismic rupture on a thrust fault, as shown in Figures 8-11. The figures show the distribution of plastic strain-rate in map view immediately after a coseismic event, and 31 days, 5 years, and 15 years after the mainshock. The stress-dependent viscosity creates a concentration of plastic strain accumulation below the rupture, toward the bottom of the seismogenic zone. The triangles indicate the faces of tetrahedra that form the curvilinear mesh of the lower crust. The thick lines with chevrons indicate the fault trace. The thin black dashed line indicates the intersection of the fault and the lower crust. The dashed white box indices the extent of the velocity-weakening region, where coseismic slip occurs.

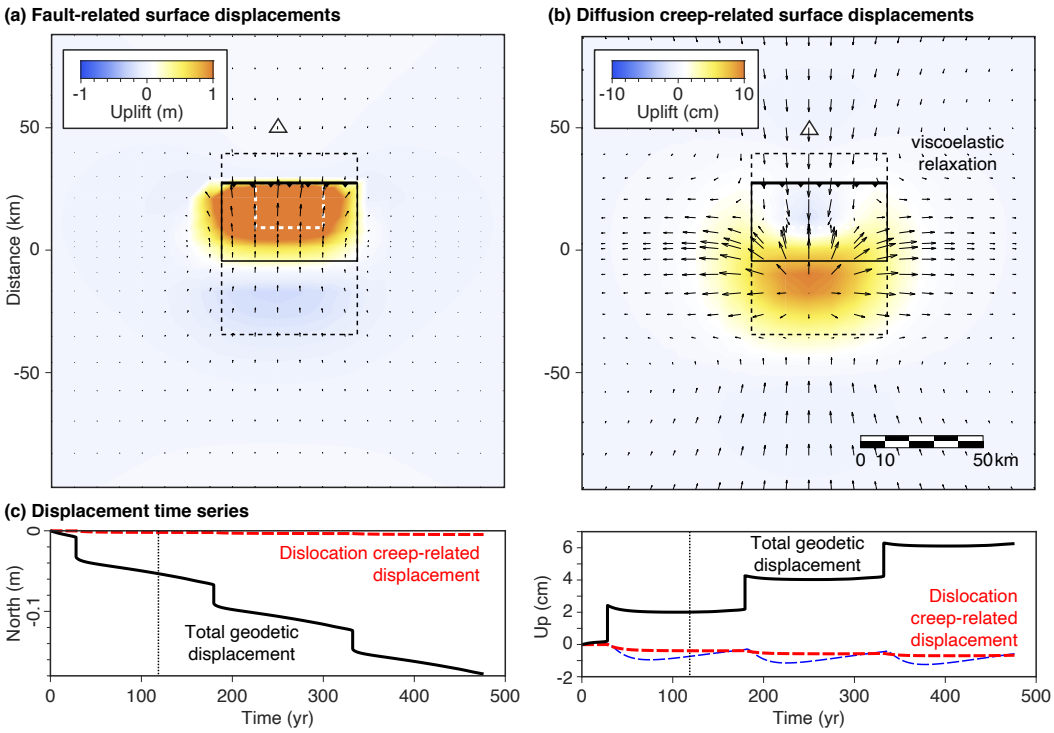

Figure 12: Crustal deformation during seismic cycles on a thrust fault overlying a viscoelastic lower crust with a nonlinear rheology. a) Cumulative surface displacement during the postseismic period showing the contribution of fault-related processes. The displacements include the effects of coseismic slip, afterslip, relocking of the seismogenic zone, and fault creep. The horizontal and vertical components are shown with arrows and background color, respectively. b) Surface displacements caused by viscoelastic flow in the lower crust. The vertical displacements are more subdued than in the case of a linear rheology. The thick segment with chevrons indicate the fault trace and the direction of motion. The boxes indicate the extents of the fault, velocity-weakening region, and the curvilinear mesh of the lower crust in map view. The triangle indicates the location of the geodetic station with the time series in c). c) Time series of displacement at the surface of the half-space. The total displacement is shown in black and the contribution of viscoelastic flow is shown in red. The viscoelastic effects for a different model with a linear rheology is shown for reference (blue line). Fault slip and viscoelastic flow induce vertical displacement in opposite or the same direction during the postseismic period depending on location.

them in detail. The integral method in two dimensions is similar as presented in Section 2.2. However, only the in-plane components of stress and strain are considered, resulting in a much smaller computational load. The surface and volume elements are considered infinite in the x_1 direction. The volume average of the stress tensor discussed in Section 2.3 becomes a surface integral.

We consider a subduction zone setting with a 300 km-long megathrust extending from the surface to 30 km depth (Figure 12). The megathrust is planar with a dip angle of 5.71°. We consider a velocity-weakening section between 20 and 30 km depth with a frictional parameter $a - b = -4 \times 10^{-3}$ surrounded by velocity-strengthening segments with $a - b = 4 \times 10^{-3}$. We assume the direct effect parameter $a = 0.01$, effective normal stress $\bar{\sigma} = 100$ MPa, and characteristic weakening distance $L = 5$ cm to be uniform. We discretize the fault with 500 m patches, resulting in 600 line elements.

We consider viscoelastic flow in the underlying oceanic asthenosphere and in the mantle wedge on the continental or arc side. For simplicity, we assume a uniform temperature profile using a cooling half space with a 60-million-year-old plate and mantle temperature of $1,400$°C. However, we separate the oceanic lithosphere from the mantle wedge by a cold, elastic slab dipping 60 degrees. We ignore the viscoelastic relaxation in the lower crust below the volcanic arc. We will compare the effects of two end-member rheology, a Maxwell viscosity and power-law flow. We discretize the domain with triangle elements with edge length of approximately 20 km, resulting in a mesh of 530 vertices and 907 surface elements. We use a background deviatoric strain-rate with $\dot{\epsilon}_{22} = -10^{-15}$/s, $\dot{\epsilon}_{23} = 0$, and $\dot{\epsilon}_{33} = 10^{-15}$/s, corresponding to horizontal shortening.

We first consider the case of a linear rheology with a linear viscosity in the ductile domains. Viscoelastic flow is thermally activated with an activation energy of 335 kJ/mol and activation volume of 4 cm^3/mol, compatible with diffusion creep in wet olivine [*Hirth and Kohlstedt*, 2003]. With the background temperature, this results in a minimum viscosity of 1.4×10^{20} Pa s. We simulate seismic cycles for a period of 950 years, producing 3 earthquakes with recurrence times of 313 and 373 years for the last two events. The seismic ruptures initiate at the bottom of the seismogenic zone and propagate upward after a long interseismic period where creep migrates into the velocity-weakening region, resulting in long-term variations of coupling. Each rupture is followed by afterslip along the megathrust and viscoelastic relaxation in the oceanic lithosphere and mantle wedge. Viscoelastic flow initially concentrates between 100 and 200 km depth in the oceanic asthenosphere below the mainshock. The peak strain-rate of 10^{-14}/s occurs at 150 km. The low strain-rate between 50 and 100 km depth is caused by the low temperature at these depths. The distribution of plastic strain-rate is stationary for a few decades, but subsequently migrates outward, returning to the background value after 300 years, compatible with a relaxation time of 140 years. During the late postseismic phase, plastic deformation accumulates more rapidly around the subducting slab. After 313 years, the relaxation is interrupted by another earthquake, implying that viscoelastic effects endure for multiple seismic cycles.

We compare these results with a simulation of seismic cycles assuming nonlinear rheology on the upper mantle. With the same physical properties for the megathrust, we assume power-law flow in the oceanic asthenosphere and mantle wedge. We take the rheological parameters for dislocation creep of wet olivine [*Hirth and Kohlstedt*, 2003], with an activation energy of 480 kJ/mol, activation volume of 11 cm^3/mol, and power exponent $n_M = 3.5$. The simulation also produces three earthquakes, but the recurrence times of 267 and 434 years for the last two events differ from the case with a linear rheology. With the stress-dependent viscosity, the plastic strain-rates attain 10^{-12}/s in the oceanic asthenosphere, much faster than in the linear case. After 4 and 33 years, the peak plastic strain-rate decays to 10^{-13}/s and 10^{-14}/s, respectively. After 64 years, viscoelastic relaxation is most active in the mantle wedge, with only small pockets of deformation in the oceanic asthenosphere. Deformation continues, albeit slowly and at great depths, when

the next earthquake happens, some 267 years after the previous mainshock. The rapid viscoelastic response by a stress-driven, initially low viscosity allows much of the viscoelastic relaxation to take place before the occurrence of the next earthquake. However, the change of pre-stress leads to a different distribution of plastic strain-rate following the second earthquake, illustrating the evolution of viscoelastic effects during seismic cycles, even at constant rheological properties. The third earthquake will happen some 434 years later, illustrating the modulation of earthquake recurrence times by viscoelastic flow.

5 Discussion

We provide a consistent methodology to simulate lithosphere dynamics and crustal deformation during seismic cycles, taking into account key aspects of lithosphere mechanics. Faulting and distributed plastic flow are incorporated using surface and volume elements, and their interactions is captured by Green's functions. Using surface elements resolves the extreme localization of deformation along fault without meshing the surrounding elastic domains. Using volume elements allows us to include viscoelastic flow in the ductile substrate. Viscoelastic flow by crystal plasticity is expected in the favorable hydrothermal conditions found in the asthenosphere below the roots of continents or in the oceanic upper mantle, below volcanic arcs at subduction zones, and near the base of the continental crust. Viscoelastic effects are routinely measured during the postseismic phase of the seismic cycle, post-glacial rebound, seasonal hydrological loads, and the desiccation of fluvial lakes. The viscosity of rock is also well understood from laboratory experiments at high-pressure, high-temperature conditions. The impact of earthquakes on lower-crustal and mantle flow is well identified, as the sudden coseismic stress change drives transient deformation in the ductile substrate. The other direction of coupling is less well understood, as the principle effect of viscoelastic relaxation is the modulation of recurrence times of large earthquakes, taking decades and centuries to unfold. This effect may explain some of the variability in paleoseismic catalogues.

The integral method is an important tools for the study of earthquake physics and crustal deformation, connecting tectonic geodesy, rocks mechanics, and rupture dynamics. The simulations capture the rupture style and recurrence patterns of earthquakes, including slow-slip events, tremors, slow earthquakes, seismic swarms, and crack-like and pulse-like ruptures. The recurrence patterns may include periodicity, multiple-periodic sequences, clustering, deterministic chaos, and super-cycles of full and partial ruptures. The variety of rupture styles emanate from the nonlinear, thermally activated constitutive behavior, fault geometry, and interactions among faults. However, the model also captures the dynamics of ductile flow, including viscoelastic relaxation and long-term migration of the brittle-ductile transition. The spatio-temporal evolution of plastic deformation is controlled by the rheology of rocks at the relevant temperatures, which is affected by grain-size, temperature, pressure, fluid content, and is modulated by seismic cycles. The interactions between fault dynamics and lithosphere deformation create an intricate mechanical system with complex interactions in space and time. The integral method allows us to resolve these effects and simulate the resulting surface deformation, allowing comparison with seismological and geodetic data.

The integral method affords a natural link with geodynamics, which provides an efficient way to simulate long-term deformation with finite strain. Admittedly, the example simulations described in this study assume simplistic long-term deformation models with a homogeneous background plastic strain-rate. In principle, the method may incorporate long-term plastic strain-rates from geodynamic simulations or geological reconstruction of local plate tectonics, providing a bridge between the time scales of geological processes and seismic cycles. These simulations may incorporate realistic long-term deformation and estimate its impact on seismic cycles. The integral method constitutes a staple toolkit to connect different aspects of lithosphere mechanics at different time scales to improve our understanding of earthquake physics. A caveat of the approach is the quasi-dynamic

approximation, producing unrealistic, slow rupture propagation. Future work should overcome this simplification.

6 Conclusions

We derive the fundamentals of the integral method to simulate the mechanical coupling between faulting and ductile processes during seismic cycles in a viscoelastic half-space. Earthquakes induce rapid stress changes in the ductile substrate that drive viscoelastic relaxation and postseismic transient deformation. The spatial distribution of viscoelastic flow in not stationary during the postseismic period, with outward migration of the initial plastic strain-rate. The quasi-static diffusion of stress by viscoelastic flow in the lower crust and asthenosphere modulates the recurrence time of earthquakes, resulting in full coupling between brittle and ductile deformation. The integral method provides a useful tool to simulate the deformation of Earth's surface during seismic cycles as the use of Green's functions accommodates observation points at arbitrary locations in the half space, regardless of the underlying mesh, with decomposition of the contributions of fault slip and viscoelastic flow. The numerical approach is derived for three-dimensional and two-dimensional cases and provide a robust, accurate, and stable numerical solution. The numerical method is implemented in an open-source software with distributed memory parallelization. Incorporating viscoelastic effects implies a higher computational burden than an elastic half-space. Future work will integrate more general volume elements to reduce the mesh size and the corresponding computational burden, and accelerate the calculation with dedicated numerical techniques. Additional work is needed to create more general surface elements with non-uniform slip distributions to incorporate structurally complex fault geometry.

7 CRediT authorship contribution statement

Conception and design of the study: S. Barbot; Formal analysis: S. Barbot; Drafting the manuscript: S. Barbot.

8 Acknowledgement

This study is supported in part by the National Science Foundation under award number EAR-1848192. We acknowledge the hospitality of the Earthquake Research Institute, University of Tokyo and the Institute of Geology, China Earthquake Administration, Beijing.

9 Code availability

The code *Unicycle* that implements the integral method for two-dimensional and three-dimensional half-spaces is available at `https://bitbucket.org/sbarbot/unicycle`.

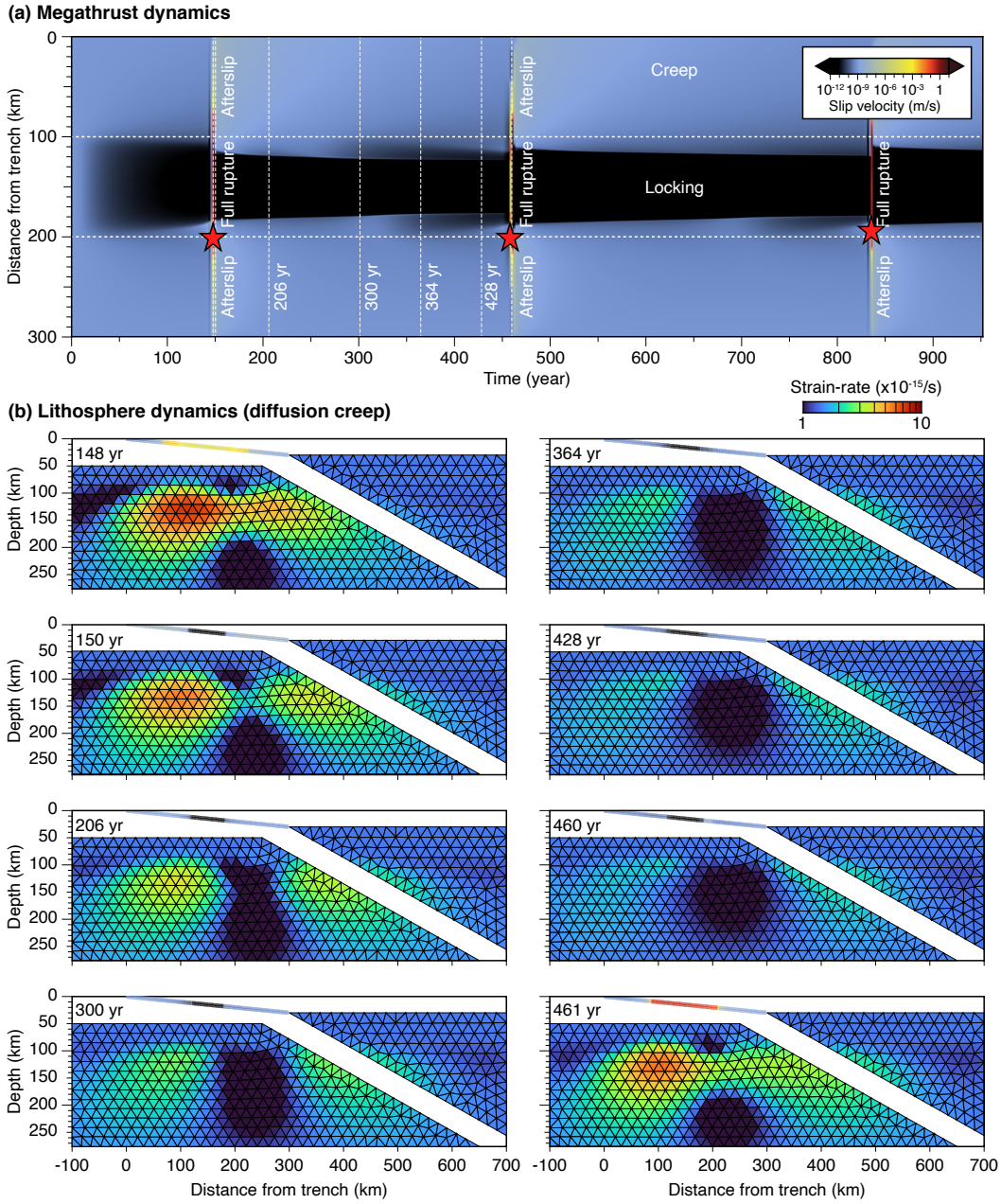

Figure 13: Seismic cycles in a subduction zone with a megathrust overlying a viscoelastic upper mantle with a linear rheology. The simulation operates in two dimensions with the in-plane strain approximation. Earthquakes develop on a 5.71°-dipping megathrust overlying a viscoelastic asthenosphere with a depth-dependent viscosity. The oceanic asthenosphere and mantle wedge are separated by a cold subducting slab dipping 60°. The rheology of the upper mantle is compatible with diffusion creep in wet olivine. a) Dynamics of slip on the megathrust for a simulation period of 950 years. The ruptures are followed by afterslip in the velocity-strengthening regions and long waves of partial coupling at the boundary of the velocity-weakening region. The stars indicate the hypocenter of earthquakes. b) Evolution of plastic strain-rate in the upper mantle during the postseismic period of the first simulated earthquake. The distribution of plastic strain-rate is modulated by the coseismic stress change and the temperature and pressure dependence of viscosity. The triangles indicate the curvilinear mesh. The slip-rate on the megathrust is indicated by colors, showing the sections of coseismic slip, afterslip, creep, and relocking.

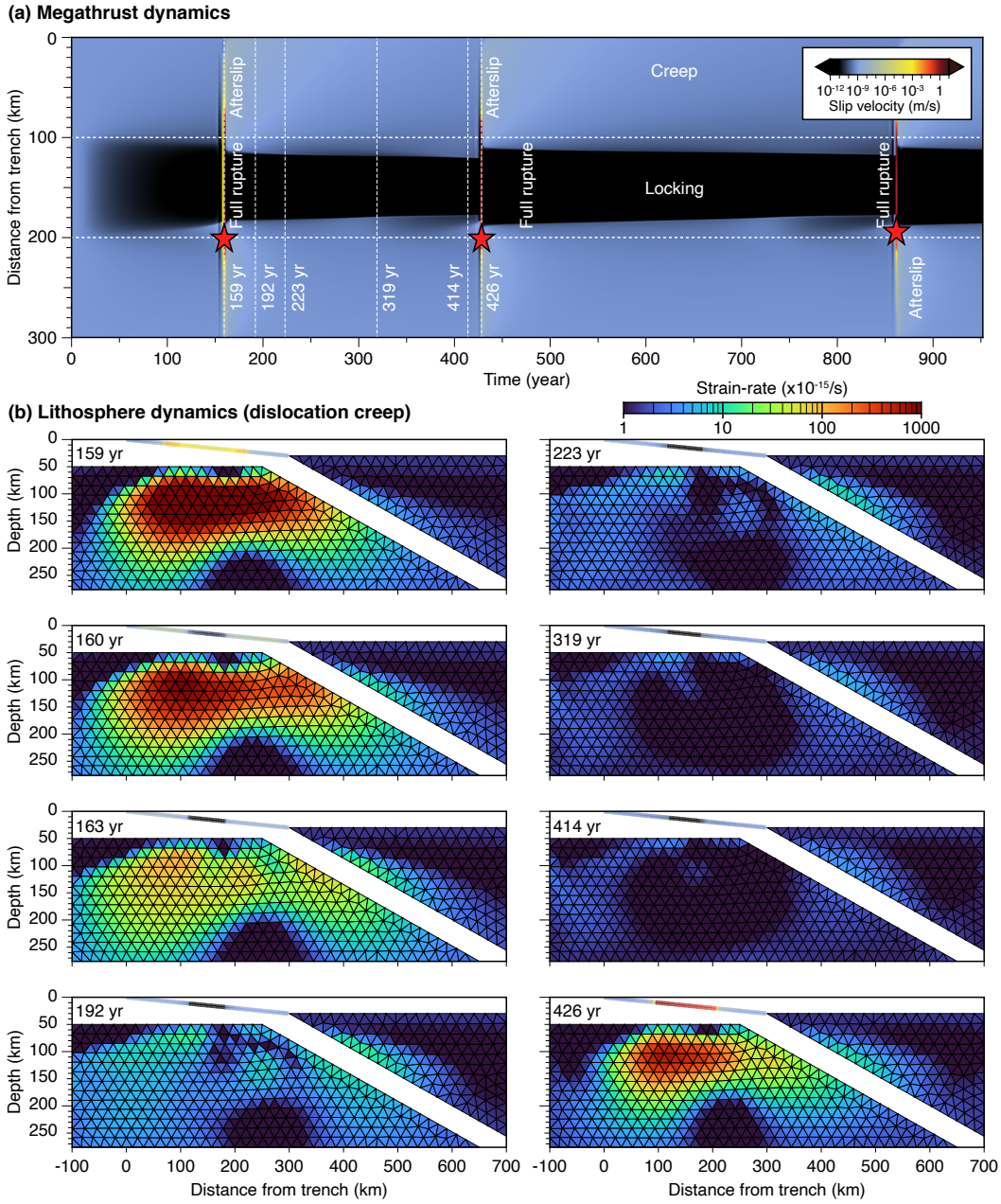

Figure 14: Seismic cycles on a megathrust overlying a viscoelastic upper mantle with a nonlinear rheology. The frictional properties of the megathrust are identical as in the previous simulation with a linear rheology (Figure 12). The rheology of the oceanic asthenosphere and mantle wedge corresponds to dislocation creep of wet olivine modulated by temperature and confining pressure. a) Dynamics of the megathrust for a period of 950 years with three seismic events (red star for hypocenter) followed by afterslip during the postseismic period and long-term creep waves at the boundary of the velocity-weakening region during the interseismic period. The background color indicates the amplitude of slip-rate. b) Distribution of plastic strain-rate in the oceanic asthenosphere and mantle wedge and slip-rate on the megathrust.

A: Appendix

In this Appendix, we describe a procedure to accelerate the calculation of stress interactions in Equations 29 and 31. The Green's functions for displacement can decomposed into terms that depend on the distance of a receiver with the source and image, as in

$$G_{ij} = G^s_{ij} + G^i_{ij} \,, \tag{A.1}$$

involving the radii

$$\begin{aligned} R_1 &= ((x_1 - y_1)^2 + (x_2 - y_2)^2 + (y_3 - x_3)^2)^{1/2} \\ R_2 &= ((x_1 - y_1)^2 + (x_2 - y_2)^2 + (x_3 + y_3)^2)^{1/2} \,, \end{aligned} \tag{A.2}$$

representing the source-receiver and the image-receiver distances, respectively. By construction, the Green's function component G^s_{ij} depends only of the distance radius R_1. Similarly, the Green's function component G^i_{ij} depends only on R_2. The Green's function for the direct effect of the source follows a simple closed-form expression

$$G^s_{ij} = \frac{1}{16\pi\mu(1-\nu)}\left[\frac{3-4\nu}{R_1}\delta_{ij} + \frac{(x_i - y_i)(x_j - y_j)}{{R_1}^3}\right] , \tag{A.3}$$

involving one term when $i \neq j$ and two terms when $i = j$. In contrast, the components of the Green's function depending on the distance with the image involve some 35 terms. For the u_1 component, they are

$$\begin{aligned} G^i_{11} = \frac{1}{16\pi\mu(1-\nu)}\Bigg[&\frac{1}{R_2} + \frac{(3-4\nu)(x_1 - y_1)^2}{{R_2}^3} \\ &+ \frac{2\,x_3 y_3\left({R_2}^2 - 3\,(x_1 - y_1)^2\right)}{{R_2}^5} \\ &+ \frac{4(1-2\nu)(1-\nu)\left({R_2}^2 - (x_1 - y_1)^2 + R_2\,(x_3 + y_3)\right)}{R_2\,(R_2 + x_3 + y_3)^2}\Bigg] , \\ G^i_{21} = \frac{(x_1 - y_1)\,(x_2 - y_2)}{16\pi\mu(1-\nu)}&\left[\frac{3-4\nu}{{R_2}^3} - \frac{6\,x_3 y_3}{{R_2}^5} - \frac{4(1-2\nu)(1-\nu)}{R_2\,(R_2 + x_3 + y_3)^2}\right] , \\ G^i_{31} = \frac{(x_1 - y_1)}{16\pi\mu(1-\nu)}&\Bigg[\frac{(3-4\nu)\,(x_3 - y_3)}{{R_2}^3} \\ &+ \frac{6\,x_3 y_3\,(x_3 + y_3)}{{R_2}^5} - \frac{4\,(1-2\nu)(1-\nu)}{R_2\,(R_2 + x_3 + y_3)}\Bigg] . \end{aligned} \tag{A.4}$$

For the u_2 component, they read

$$\begin{aligned} G^i_{12} = \frac{(x_1 - y_1)\,(x_2 - y_2)}{16\pi\mu(1-\nu)}&\left[\frac{3-4\nu}{{R_2}^3} - \frac{6\,x_3 y_3}{{R_2}^5} - \frac{4(1-2\nu)(1-\nu)}{R_2\,(R_2 + x_3 + y_3)^2}\right] , \\ G^i_{22} = \frac{1}{16\pi\mu(1-\nu)}&\Bigg[\frac{1}{R_2} + \frac{(3-4\nu)\,(x_2 - y_2)^2}{{R_2}^3} \\ &+ \frac{2\,x_3 y_3\left({R_2}^2 - 3\,(x_2 - y_2)^2\right)}{{R_2}^5} \\ &+ \frac{4(1-2\nu)(1-\nu)\left({R_2}^2 - (x_2 - y_2)^2 + R_2\,(x_3 + y_3)\right)}{R_2\,(R_2 + x_3 + y_3)^2}\Bigg] , \\ G^i_{32} = \frac{(x_2 - y_2)}{16\pi\mu(1-\nu)}&\Bigg[\frac{(3-4\nu)\,(x_3 - y_3)}{{R_2}^3} \\ &+ \frac{6\,x_3 y_3\,(x_3 + y_3)}{{R_2}^5} - \frac{4\,(1-2\nu)(1-\nu)}{R_2\,(R_2 + x_3 + y_3)}\Bigg] . \end{aligned} \tag{A.5}$$

For the displacement component u_3, they are given by

$$
\begin{aligned}
G^i_{13} &= \frac{(x_1 - y_1)}{16\pi\mu(1-\nu)}\left[\frac{(3-4\nu)\,(x_3 - y_3)}{{R_2}^3}\right. \\
&\qquad \left. - \frac{6\,x_3 y_3\,(x_3 + y_3)}{{R_2}^5} + \frac{4(1-2\nu)(1-\nu)}{R_2\,(R_2 + x_3 + y_3)}\right], \\
G^i_{23} &= \frac{(x_2 - y_2)}{16\pi\mu(1-\nu)}\left[\frac{(3-4\nu)\,(x_3 - y_3)}{{R_2}^3}\right. \\
&\qquad \left. - \frac{6\,x_3 y_3\,(x_3 + y_3)}{{R_2}^5} + \frac{4(1-2\nu)(1-\nu)}{R_2\,(R_2 + x_3 + y_3)}\right] \\
G^i_{33} &= \frac{1}{16\pi\mu(1-\nu)}\left[\frac{5 - 12\nu + 8\nu^2}{R_2}\right. \\
&\qquad \left. + \frac{6\,x_3 y_3\,(x_3 + y_3)^2}{{R_2}^5} + \frac{(3-4\nu)\,(x_3 + y_3)^2 - 2\,x_3 y_3}{{R_2}^3}\right].
\end{aligned}
\tag{A.6}
$$

The image-receiver distance is always greater than the source-receiver distance, especially if the source is confined at great depth. We take advantage of this situation by using a low-order quadrature for the Green's function components depending on the source-image distance and a high-order quadrature for the Green's function components that depend on the source-receiver distance. For the calculation of displacements, this leads to an acceleration of the Green's function calculation by an order of magnitude without loss of accuracy.

A similar approach can be devised for the calculations of the displacement gradient, which is used to evaluate stress and traction. The Green's function for the displacement gradient can also be decomposed in terms of distance of the receiver from the source and from the image, as follows

$$
G_{ij,k} = G^s_{ij,k} + G^i_{ij,k}\ , \tag{A.7}
$$

where the Green's function $G^s_{ij,k}$ depends only on the distance from the source R_1 and $G^i_{ij,k}$ depends only on the distance from the image. The direct effect of the source follows the expression

$$
\begin{aligned}
G^s_{ij,k} = \frac{1}{16\pi\mu(1-\nu)}\Bigg[&- (3-4\nu)\frac{x_k - y_k}{R_1^3}\delta_{ij} \\
&+ \frac{(\delta_{ik} r_j + \delta_{jk} r_i) R_1^2 - 3(x_i - y_i)(x_j - y_j)(x_k - y_k)}{R_1^5}\Bigg]
\end{aligned}
\tag{A.8}
$$

containing 1 to 4 terms per component. The other part of the Green's function that depends on the distance with the image are given below. For the derivatives of the G^i_{11} com-

ponent, we have

$$
\begin{aligned}
G^i_{11,1} = \frac{(x_1-y_1)}{16\pi\mu(1-\nu)}\Bigg[& -\frac{1}{{R_2}^3} + (3-4\,\nu)\,\frac{2{R_2}^2 - 3\,(x_1-y_1)^2}{{R_2}^5} - 6\,y_3\,x_3\frac{3{R_2}^2 - 5(x_1-y_1)^2}{{R_2}^7} \\
& - 12\frac{(1-2\nu)\,(1-\nu)}{R_2\,(R_2+x_3+y_3)^2} \\
& + \frac{4\,(1-2\nu)(1-\nu)\,(x_1-y_1)^2}{{R_2}^3\,(R_2+x_3+y_3)^2} + \frac{8\,(1-2\nu)(1-\nu)\,(x_1-y_1)^2}{{R_2}^2\,(R_2+x_3+y_3)^3}\Bigg], \\
G^i_{11,2} = \frac{(x_2-y_2)}{16\pi\mu(1-\nu)}\Bigg[& -\frac{1}{{R_2}^3} - \frac{3\,(3-4\,\nu)\,(x_1-y_1)^2}{{R_2}^5} \\
& - 6\,y_3\,x_3\,\frac{{R_2}^2 - 5(x_1-y_1)^2}{{R_2}^7} - \frac{4\,(1-2\nu)\,(1-\nu)}{R_2\,(R_2+x_3+y_3)^2} \\
& + 4\,(1-2\nu)\,(1-\nu)\,(x_1-y_1)^2\,\frac{3R_2+x_3+y_3}{{R_2}^3\,(R_2+x_3+y_3)^3}\Bigg], \\
G^i_{11,3} = \frac{1}{16\pi\mu(1-\nu)}\Bigg[& -\frac{(x_3+y_3)}{{R_2}^3} - 3\,\frac{(3-4\,\nu)\,(x_1-y_1)^2\,(x_3+y_3)}{{R_2}^5} \\
& + 2\,y_3\,\frac{{R_2}^2 - 3\,x_3(x_3+y_3)}{{R_2}^5} \\
& - 6\,y_3\,(x_1-y_1)^2\,\frac{{R_2}^2 - 5\,x_3(x_3+y_3)}{{R_2}^7} \\
& - 4\,\frac{(1-2\nu)\,(1-\nu)}{R_2\,(R_2+x_3+y_3)} \\
& + 4\,(1-2\nu)\,(1-\nu)\,(x_1-y_1)^2\,\frac{2R_2+x_3+y_3}{{R_2}^3\,(R_2+x_3+y_3)^2}\Bigg],
\end{aligned}
\tag{A.9}
$$

and

$$
\begin{aligned}
G^i_{21,1} = \frac{(x_2-y_2)}{16\pi\mu(1-\nu)}\Bigg[& (3-4\nu)\,\frac{{R_2}^2 - 3(x_1-y_1)^2}{{R_2}^5} \\
& - 6\,y_3\,x_3\frac{{R_2}^2 - 5(x_1-y_1)^2}{{R_2}^7} - \frac{4(1-2\nu)(1-\nu)}{R_2(R_2+x_3+y_3)^2} \\
& + 4\,(1-2\nu)(1-\nu)\,(x_1-y_1)^2\,\frac{3R_2+x_3+y_3}{{R_2}^3(R_2+x_3+y_3)^3}\Bigg], \\
G^i_{21,2} = \frac{(x_1-y_1)}{16\pi\mu(1-\nu)}\Bigg[& (3-4\nu)\,\frac{{R_2}^2 - 3(x_2-y_2)^2}{{R_2}^5} \\
& - 6\,y_3\,x_3\,\frac{{R_2}^2 - 5(x_2-y_2)^2}{{R_2}^7} - \frac{4(1-2\nu)(1-\nu)}{R_2(R_2+x_3+y_3)^2} \\
& + 4(1-2\nu)(1-\nu)(x_2-y_2)^2\frac{3R_2+x_3+y_3}{{R_2}^3(R_2+x_3+y_3)^3}\Bigg], \\
G^i_{21,3} = \frac{(x_1-y_1)\,(x_2-y_2)}{16\pi\mu(1-\nu)}\Bigg[& -3\,(3-4\nu)\,\frac{(x_3+y_3)}{{R_2}^5} \\
& - 6\,y_3\frac{{R_2}^2 - 5\,x_3\,(x_3+y_3)}{{R_2}^7} \\
& + 4\,(1-2\nu)\,(1-\nu)\,\frac{2R_2+x_3+y_3}{{R_2}^3\,(R_2+x_3+y_3)^2}\Bigg].
\end{aligned}
\tag{A.10}
$$

Continuing for the derivatives of G^i_{31},

$$
\begin{aligned}
G^i_{31,1} = \frac{1}{16\pi\mu(1-\nu)}\Bigg[&(3-4\nu)(x_3-y_3)\frac{{R_2}^2-3(x_1-y_1)^2}{{R_2}^5}\\
&+6\,x_3\,y_3\,(x_3+y_3)\frac{{R_2}^2-5(x_1-y_1)^2}{{R_2}^7}\\
&-4\,(1-2\nu)(1-\nu)\frac{1}{R_2(R_2+x_3+y_3)}\\
&+4\,(1-2\nu)(1-\nu)(x_1-y_1)^2\frac{2R_2+x_3+y_3}{{R_2}^3(R_2+x_3+y_3)^2}\Bigg],\\
G^i_{31,2} = \frac{(x_1-y_1)(x_2-y_2)}{16\pi\mu(1-\nu)}\Bigg[&-3(3-4\nu)\frac{(x_3-y_3)}{{R_2}^5}\\
&-30\,y_3\,x_3\frac{(x_3+y_3)}{{R_2}^7}+4(1-2\nu)(1-\nu)\frac{2R_2+x_3+y_3}{{R_2}^3(R_2+x_3+y_3)^2}\Bigg],\\
G^i_{31,3} = \frac{(x_1-y_1)}{16\pi\mu(1-\nu)}\Bigg[&+(3-4\nu)\frac{{R_2}^2-3(x_3+y_3)(x_3-y_3)}{{R_2}^5}\\
&+6\,y_3\frac{{R_2}^2(2x_3+y_3)-5x_3(x_3+y_3)^2}{{R_2}^7}+4\frac{(1-2\nu)(1-\nu)}{{R_2}^3}\Bigg].
\end{aligned}
\tag{A.11}
$$

The derivatives of the G^i_{12} component are the same as for G^i_{21} component, given by

$$
\begin{aligned}
G^i_{12,1} = \frac{(x_2-y_2)}{16\pi\mu(1-\nu)}\Bigg[&+(3-4\nu)\frac{{R_2}^2-3(x_1-y_1)^2}{{R_2}^5}\\
&-6\,y_3\,x_3\,\frac{{R_2}^2-5(x_1-y_1)^2}{{R_2}^7}-\frac{4(1-\nu)(1-2\nu)}{R_2(R_2+x_3+y_3)^2}\\
&+4(1-\nu)(1-2\nu)(x_1-y_1)^2\frac{3R_2+x_3+y_3}{{R_2}^3(R_2+x_3+y_3)^3}\Bigg],\\
G^i_{12,2} = \frac{(x_1-y_1)}{16\pi\mu(1-\nu)}\Bigg[&+(3-4\nu)\frac{{R_2}^2-3(x_2-y_2)^2}{{R_2}^5}\\
&-6\,y_3\,x_3\frac{{R_2}^2-5(x_2-y_2)^2}{{R_2}^7}-\frac{4(1-\nu)(1-2\nu)}{R_2(R_2+x_3+y_3)^2}\\
&+4(1-\nu)(1-2\nu)\,(x_2-y_2)^2\frac{3R_2+x_3+y_3}{{R_2}^3(R_2+x_3+y_3)^3}\Bigg],\\
G^i_{12,3} = \frac{(x_1-y_1)\,(x_2-y_2)}{16\pi\mu(1-\nu)}\Bigg[&-3\,(3-4\nu)\,\frac{(x_3+y_3)}{{R_2}^5}\\
&-6\,y_3\frac{{R_2}^2-5\,x_3\,(x_3+y_3)}{{R_2}^7}\\
&+4\,(1-2\nu)\,(1-\nu)\,\frac{2R_2+x_3+y_3}{{R_2}^3\,(R_2+x_3+y_3)^2}\Bigg].
\end{aligned}
\tag{A.12}
$$

The derivatives of the G^i_{22} can be obtained exploiting the symmetry with those of the G^i_{11} component by permutation of the 1 and 2 indices, giving the following expressions

$$
\begin{aligned}
G^i_{22,1} = \frac{(x_1 - y_1)}{16\pi\mu(1-\nu)}\Bigg[& -\frac{1}{{R_2}^3} - \frac{3\,(3-4\,\nu)\,(x_2-y_2)^2}{{R_2}^5} \\
& - 6\,y_3\,x_3\,\frac{{R_2}^2 - 5(x_2-y_2)^2}{{R_2}^7} - \frac{4\,(1-2\nu)\,(1-\nu)}{R_2\,(R_2+x_3+y_3)^2} \\
& + 4\,(1-2\nu)\,(1-\nu)\,(x_2-y_2)^2\,\frac{3R_2+x_3+y_3}{{R_2}^3\,(R_2+x_3+y_3)^3}\Bigg], \\
G^i_{22,2} = \frac{(x_2 - y_2)}{16\pi\mu(1-\nu)}\Bigg[& -\frac{1}{{R_2}^3} + (3-4\,\nu)\,\frac{2{R_2}^2 - 3\,(x_2-y_2)^2}{{R_2}^5} - 6\,y_3\,x_3\frac{3{R_2}^2 - 5(x_2-y_2)^2}{{R_2}^7} \\
& - 12\frac{(1-2\nu)\,(1-\nu)}{R_2\,(R_2+x_3+y_3)^2} \\
& + 4\,(1-2\nu)\,(1-\nu)\,(x_2-y_2)^2\,\frac{3R_2+x_3+y_3}{{R_2}^3\,(R_2+x_3+y_3)^3}\Bigg], \\
G^i_{22,3} = \frac{1}{16\pi\mu(1-\nu)}\Bigg[& -\frac{(x_3+y_3)}{{R_2}^3} - 3\,(3-4\,\nu)\,\frac{(x_2-y_2)^2\,(x_3+y_3)}{{R_2}^5} \\
& + 2\,y_3\,\frac{{R_2}^2 - 3\,x_3(x_3+y_3)}{{R_2}^5} \\
& - 6\,y_3\,(x_2-y_2)^2\,\frac{{R_2}^2 - 5\,x_3(x_3+y_3)}{{R_2}^7} \\
& - 4\frac{(1-2\nu)\,(1-\nu)}{R_2\,(R_2+x_3+y_3)} \\
& + 4\,(1-2\nu)\,(1-\nu)\,(x_2-y_2)^2\,\frac{2R_2+x_3+y_3}{{R_2}^3\,(R_2+x_3+y_3)^2}\Bigg],
\end{aligned}
\tag{A.13}
$$

Similarly, the derivatives of the G^i_{32} term can be obtained from the G^i_{31} term by permutation of the 1 and 2 indices, given us

$$
\begin{aligned}
G^i_{32,1} = \frac{(x_1 - y_1)(x_2 - y_2)}{16\pi\mu(1-\nu)}\Bigg[& -3(3-4\nu)\frac{(x_3-y_3)}{{R_2}^5} \\
& - 30\,y_3\,x_3\frac{(x_3+y_3)}{{R_2}^7} + 4(1-2\nu)(1-\nu)\frac{2R_2+x_3+y_3}{{R_2}^3(R_2+x_3+y_3)^2}\Bigg], \\
G^i_{32,2} = \frac{1}{16\pi\mu(1-\nu)}\Bigg[& (3-4\nu)(x_3-y_3)\frac{{R_2}^2 - 3(x_2-y_2)^2}{{R_2}^5} \\
& + 6\,y_3\,x_3\,(x_3+y_3)\frac{{R_2}^2 - 5(x_2-y_2)^2}{{R_2}^7} \\
& - 4\,(1-2\nu)\,(1-\nu)\,\frac{1}{R_2(R_2+x_3+y_3)} \\
& + 4\,(1-2\nu)\,(1-\nu)\,(x_2-y_2)^2\,\frac{2R_2+x_3+y_3}{{R_2}^3(R_2+x_3+y_3)^2}\Bigg], \\
G^i_{32,3} = \frac{(x_2 - y_2)}{16\pi\mu(1-\nu)}\Bigg[& +(3-4\nu)\frac{{R_2}^2 - 3(x_3-y_3)(x_3+y_3)}{{R_2}^5} \\
& + 6\,y_3\frac{(2x_3+y_3)}{{R_2}^5} - 30\,y_3\,x_3\frac{(x_3+y_3)^2}{{R_2}^7} + 4\frac{(1-2\nu)(1-\nu)}{{R_2}^3}\Bigg].
\end{aligned}
\tag{A.14}
$$

951 The derivatives of the Green's function component G^i_{13} are given by

$$
\begin{aligned}
G^i_{13,1} &= \frac{1}{16\pi\mu(1-\nu)}\Bigg[(3-4\nu)\,(x_3-y_3)\,\frac{{R_2}^2-3(x_1-y_1)^2}{{R_2}^5} \\
&\quad - 6\,y_3\,x_3\,(x_3+y_3)\,\frac{{R_2}^2-5(x_1-y_1)^2}{{R_2}^7} + \frac{4(1-2\nu)(1-\nu)}{R_2(R_2+x_3+y_3)} \\
&\quad - 4(1-2\nu)(1-\nu)(x_1-y_1)^2\,\frac{2R_2+x_3+y_3}{{R_2}^3(R_2+x_3+y_3)^2}\Bigg], \\
G^i_{13,2} &= \frac{(x_1-y_1)(x_2-y_2)}{16\pi\mu(1-\nu)}\Bigg[-3\,(3-4\nu)\,(x_3-y_3)\frac{1}{{R_2}^5} \\
&\quad + 30\,y_3\,x_3\,(x_3+y_3)\frac{1}{{R_2}^7} \\
&\quad - 4(1-2\nu)(1-\nu)\frac{2R_2+x_3+y_3}{{R_2}^3(R_2+x_3+y_3)^2}\Bigg], \\
G^i_{13,3} &= \frac{(x_1-y_1)}{16\pi\mu(1-\nu)}\Bigg[(3-4\nu)\frac{{R_2}^2-3(x_3-y_3)(x_3+y_3)}{{R_2}^5} \\
&\quad - 6\,y_3\frac{2x_3+y_3}{{R_2}^5} + 30\,y_3\,x_3\frac{(x_3+y_3)^2}{{R_2}^7} \\
&\quad - 4(1-2\nu)(1-\nu)\frac{1}{{R_2}^3}\Bigg].
\end{aligned}
\tag{A.15}
$$

952 The derivatives of the G^i_{23} can be obtained from the G^i_{13} derivatives by permutation of the
953 1 and 2 indices, providing

$$
\begin{aligned}
G^i_{23,1} &= \frac{(x_1-y_1)(x_2-y_2)}{16\pi\mu(1-\nu)}\Bigg[-3\,(3-4\nu)\,(x_3-y_3)\frac{1}{{R_2}^5} \\
&\quad + 30\,y_3\,x_3\,(x_3+y_3)\frac{1}{{R_2}^7} \\
&\quad - 4(1-2\nu)(1-\nu)\frac{2R_2+x_3+y_3}{{R_2}^3(R_2+x_3+y_3)^2}\Bigg], \\
G^i_{23,2} &= \frac{1}{16\pi\mu(1-\nu)}\Bigg[(3-4\nu)\,(x_3-y_3)\,\frac{{R_2}^2-3(x_2-y_2)^2}{{R_2}^5} \\
&\quad - 6\,y_3\,x_3\,(x_3+y_3)\,\frac{{R_2}^2-5(x_2-y_2)^2}{{R_2}^7} + \frac{4(1-2\nu)(1-\nu)}{R_2(R_2+x_3+y_3)} \\
&\quad - 4(1-2\nu)(1-\nu)(x_2-y_2)^2\,\frac{2R_2+x_3+y_3}{{R_2}^3(R_2+x_3+y_3)^2}\Bigg], \\
G^i_{23,3} &= \frac{(x_2-y_2)}{16\pi\mu(1-\nu)}\Bigg[(3-4\nu)\frac{{R_2}^2-3(x_3-y_3)(x_3+y_3)}{{R_2}^5} \\
&\quad - 6\,y_3\frac{2x_3+y_3}{{R_2}^5} + 6\,y_3\,x_3\frac{(x_3+y_3)^2}{{R_2}^7} \\
&\quad - 4(1-2\nu)(1-\nu)\frac{1}{{R_2}^3}\Bigg].
\end{aligned}
\tag{A.16}
$$

Finally, the derivatives of the G^i_{33} component are given by

$$
\begin{aligned}
G^i_{33,1} &= \frac{(x_1 - y_1)}{16\pi\mu(1-\nu)}\Bigg[-(5 - 12\nu + 8\nu^2)\frac{1}{{R_2}^3} \\
&\quad - 30\, y_3\, x_3 \frac{(x_3 + y_3)^2}{{R_2}^7} - 3(3 - 4\nu)\frac{(x_3 + y_3)^2}{{R_2}^5} + 6\frac{y_3 x_3}{{R_2}^5}\Bigg] , \\
G^i_{33,2} &= \frac{(x_2 - y_2)}{16\pi\mu(1-\nu)}\Bigg[-(5 - 12\nu + 8\nu^2)\frac{1}{{R_2}^3} \\
&\quad - 30\, y_3\, x_3 \frac{(x_3 + y_3)^2}{{R_2}^7} - 3(3 - 4\nu)\frac{(x_3 + y_3)^2}{{R_2}^5} + 6\frac{y_3 x_3}{{R_2}^5}\Bigg] , \\
G^i_{33,3} &= \frac{1}{16\pi\mu(1-\nu)}\Bigg[-(5 - 12\nu + 8\nu^2)\frac{(x_3 + y_3)}{{R_2}^3} \\
&\quad + 6\, y_3 \frac{(x_3 + y_3)^2}{{R_2}^5} \\
&\quad + 6\, y_3\, x_3\, (x_3 + y_3)\frac{2{R_2}^2 - 5(x_3 + y_3)^2}{{R_2}^7} \\
&\quad + (3 - 4\nu)\,(x_3 + y_3)\frac{2{R_2}^2 - 3(x_3 + y_3)^2}{{R_2}^5} \\
&\quad - 2\, y_3 \frac{{R_2}^2 - 3x_3(x_3 + y_3)}{{R_2}^5}\Bigg] .
\end{aligned}
\tag{A.17}
$$

The Green's function components $G^i_{ij,k}$ contain another 158 terms. Hence, using a high-order quadrature for the source terms and a low-order quadrature for the image terms accelerate the calculation by a factor of about 2 to 3. We use this approach to optimize the calculation of Green's functions for displacement and deformation without loss of numerical accuracy.

References

Aagaard, B. T., M. G. Knepley, and C. A. Williams (2013), A domain decomposition approach to implementing fault slip in finite-element models of quasi-static and dynamic crustal deformation, *J. Geophys. Res.*, *118*(6), 3059–3079.

Agata, R., S. D. Barbot, K. Fujita, M. Hyodo, T. Iinuma, R. Nakata, T. Ichimura, and T. Hori (2019), Rapid mantle flow with power-law creep explains deformation after the 2011 tohoku mega-quake, *Nature Communications*, *10*(1), 1385, doi:10.1038/s41467-019-08984-7.

Aki, K., and P. G. Richards (1980), *Quantitative Seismology*, vol. I, W. H. Freeman and company, New York.

Allison, K. L., and E. M. Dunham (2018), Earthquake cycle simulations with rate-and-state friction and power-law viscoelasticity, *Tectonophysics*, *733*, 232–256, doi:10.1016/j.tecto.2017.10.021.

Allison, K. L., and E. M. Dunham (2021), Influence of shear heating and thermomechanical coupling on earthquake sequences and the brittle-ductile transition, *J. Geophys. Res.*, *126*(6), e2020JB021,394, doi:10.1029/2020JB021394.

Ando, R. (2016), Fast Domain Partitioning Method for dynamic boundary integral equations applicable to non-planar faults dipping in 3-D elastic half-space, *Geophys. J. Int.*, *207*(2), 833–847, doi:10.1093/gji/ggw299.

Andrews, D. (1985), Dynamic plane-strain shear rupture with a slip-weakening friction law calculated by a boundary integral method, *Bull. Seism. Soc. Am.*, *75*(1), 1–21.

Barbot, S. (2018a), Deformation of a half-space from anelastic strain confined in a tetrahedral volume, *Bull. Seism. Soc. Am.*, *108*(5A), 2687, doi:10.1785/0120180058.

Barbot, S. (2018b), Asthenosphere flow modulated by megathrust earthquake cycles, *Geophys. Res. Lett.*, *45*, 6018–6031, doi:10.1029/2018GL078197.

Barbot, S. (2019), Modulation of fault strength during the seismic cycle by grain-size evolution around contact junctions, *Tectonophysics*, *765*, 129–145, doi:10.1016/j.tecto.2019.05.004.

Barbot, S. (2020a), Frictional and structural controls of seismic super-cycles at the Japan trench, *Earth Planets Space*, *72*(63), doi:10.1186/s40623-020-01185-3.

Barbot, S. (2020b), Mantle flow distribution beneath the California margin, *Nature Communications*, *11*(1), 1–14, doi:10.1038/s41467-020-18260-8.

Barbot, S. (2021), A spectral boundary-integral method for quasi-dynamic ruptures of multiple parallel faults, *Bull. Seism. Soc. Am.*, *111*(3), 1614–1630, doi:10.1785/0120210004.

Barbot, S. (2022), A rate-, state-, and temperature-dependent friction law with competing healing mechanisms, *J. Geophys. Res.*, *127*, e2022JB025,106, doi:10.1029/2022JB025106.

Barbot, S. (submitted), Unicycle: A integral method for seismic cycles in viscoelastic media, *J. Open Source Software*.

Barbot, S., and Y. Fialko (2010a), Fourier-domain Green's function for an elastic semi-infinite solid under gravity, with applications to earthquake and volcano deformation, *Geophys. J. Int.*, *182*(2), 568–582, doi:10.1111/j.1365-246X.2010.04655.x.

Barbot, S., and Y. Fialko (2010b), A unified continuum representation of postseismic relaxation mechanisms: semi-analytic models of afterslip, poroelastic rebound and viscoelastic flow, *Geophys. J. Int.*, *182*(3), 1124–1140, doi:10.1111/j.1365-246X.2010.04678.x.

Barbot, S., and J. Weiss (2021), Connecting subduction, extension and shear localization across the Aegean Sea and Anatolia, *Geophys. J. Int.*, *226*(1), 422–445, doi:10.1093/gji/ggab078.

Barbot, S., Y. Hamiel, and Y. Fialko (2008), Space geodetic investigation of the coseismic and postseismic deformation due to the 2003 Mw 7.2 Altai earthquake: Implications for the local lithospheric rheology, *J. Geophys. Res.*, *113*(B03403), doi:10.1029/2007JB005063.

Barbot, S., Y. Fialko, and Y. Bock (2009), Postseismic Deformation due to the Mw 6.0 2004 Parkfield Earthquake: Stress-Driven Creep on a Fault with Spatially Variable Rate-and-State Friction Parameters, *J. Geophys. Res.*, *114*(B07405), doi:10.1029/2008JB005748.

Barbot, S., N. Lapusta, and J. P. Avouac (2012), Under the hood of the earthquake machine: Towards predictive modeling of the seismic cycle, *Science*, *336*(6082), 707–710, doi:10.1126/science.1218796.

Barbot, S., J. D. Moore, and V. Lambert (2017), Displacement and stress associated with distributed anelastic deformation in a half-space, *Bull. Seism. Soc. Am.*, *107*(2), 821–855, doi:10.1785/0120160237.

Bedford, J., M. Moreno, S. Li, O. Oncken, J. C. Baez, M. Bevis, O. Heidbach, and D. Lange (2016), Separating rapid relocking, afterslip, and viscoelastic relaxation: An application of the postseismic straightening method to the maule 2010 cgps, *J. Geophys. Res.*, *121*(10), 7618–7638.

Biemiller, J., and L. Lavier (2017), Earthquake supercycles as part of a spectrum of normal fault slip styles, *J. Geophys. Res.*, *122*(4), 3221–3240.

Blanpied, M., C. Marone, D. Lockner, J. Byerlee, and D. King (1998), Quantitative measure of the variation in fault rheology due to fluid-rock interactions, *J. Geophys. Res.*, *103*(B5), 9691–9712, doi:10.1029/98JB00162.

Blanpied, M. L., D. A. Lockner, and J. D. Byerlee (1995), Frictional slip of granite at hydrothermal conditions, *J. Geophys. Res.*, *100*(B7), 13,045–13,064, doi:10.1029/95JB00862.

Bradley, A. M. (2014), Software for efficient static dislocation–traction calculations in fault simulators, *Seism. Res. Lett.*, *85*(6), 1358–1365, doi:10.1785/0220140092.

Broerse, T., R. Riva, W. Simons, R. Govers, and B. Vermeersen (2015), Postseismic grace and gps observations indicate a rheology contrast above and below the sumatra slab, *J. Geophys. Res.*, *120*(7), 5343–5361.

Bürgmann, R., and G. Dresen (2008), Rheology of the lower crust and upper mantle: Evidence from rock mechanics, geodesy, and field observations, *Ann. Rev. Earth Plan. Sc.*, *36*, 531–567, doi:10.1146/annurev.earth.36.031207.124326.

Burov, E. B., and A. B. Watts (2006), The long-term strength of continental lithosphere: "jelly sandwich" or "crême brûlée"?, *GSA Today*, *16*(1).

Chen, X., and H. Zhang (2006), Modelling rupture dynamics of a planar fault in 3-d half space by boundary integral equation method: An overview, *Pure Appl. Geophys.*, *163*(2-3), 267–299, doi:10.1007/s00024-005-0020-z.

Chen, Y., M. Liu, and G. Luo (2020), Complex temporal patterns of large earthquakes: Devil's staircases, *Bull. Seism. Soc. Am.*, *110*(3), 1064–1076, doi:10.1785/0120190148.

Chester, F. M. (1994), Effects of temperature on friction: Constitutive equations and experiments with fault gouge, *J. Geophys. Res.*, *99*(B4), 7247–7261, doi:10.1029/93JB03110.

Chester, F. M., and J. S. Chester (1998), Ultracataclasite structure and friction processes of the Punchbowl fault, San Andreas system, California, *Tectonophysics*, *295*, 199–221.

Chopra, P. N. (1997), High-temperature transient creep in olivine rocks, *Tectonophysics*, *279*(104), 93–111.

Chuang, R. Y., and K. M. Johnson (2011), Reconciling geologic and geodetic model fault slip-rate discrepancies in Southern California: Consideration of nonsteady mantle flow and lower crustal fault creep, *Geology*, *39*(7), 627–630, doi:10.1130/G32120.1.

Comninou, M., and J. Dundurs (1975), The angular dislocation in a half space, *Journal of Elasticity*, *5*(3-4), 203–216.

Dal Zilio, L., Y. van Dinther, T. Gerya, and J.-P. Avouac (2019), Bimodal seismicity in the himalaya controlled by fault friction and geometry, *Nature Communications*, *10*(1), 48.

Day, S. M. (1982), Three-dimensional finite difference simulation of fault dynamics: rectangular faults with fixed rupture velocity, *Bull. Seism. Soc. Am.*, *72*(3), 705–727.

Day, S. M., L. A. Dalguer, N. Lapusta, and Y. Liu (2005), Comparison of finite difference and boundary integral solutions to three-dimensional spontaneous rupture, *J. Geophys. Res.*, *110*(B12307).

Diao, F., R. Wang, Y. Wang, X. Xiong, and T. R. Walter (2018), Fault behavior and lower crustal rheology inferred from the first seven years of postseismic GPS data after the 2008 Wenchuan earthquake, *Earth Planet. Sci. Lett.*, *495*, 202–212, doi:10.1016/j.epsl.2018.05.020.

Dimanov, A., and G. Dresen (2005), Rheology of synthetic anorthite-diopside aggregates: Implications for ductile shear zones, *J. Geophys. Res.*, *110*(B7), doi:10.1029/2004JB003431.

Dinther, Y. v., T. V. Gerya, L. A. Dalguer, P. M. Mai, G. Morra, and D. Giardini (2013), The seismic cycle at subduction thrusts: Insights from seismo-thermo-mechanical models, *J. Geophys. Res.*, *118*(12), 6183–6202, doi:10.1002/2013JB010380.

Dublanchet, P. (2017), The dynamics of earthquake precursors controlled by effective friction, *Geophys. J. Int.*, *212*(2), 853–871.

Dublanchet, P., P. Bernard, and P. Favreau (2013), Interactions and triggering in a 3-d rate-and-state asperity model, *J. Geophys. Res.*, *118*(5), 2225–2245, doi:10.1002/jgrb.50187.

Ellis, S., and B. Stöckhert (2004), Imposed strain localization in the lower crust on seismic timescales, *Earth Planets Space*, *56*(12), 1103–1109, doi:10.1186/BF03353329.

Erickson, B., J. Jiang, M. Barall, N. Lapusta, E. Dunham, R. Harris, L. Abrahams, K. Allison, J.-P. Ampuero, S. Barbot, et al. (2020), The Community Code Verification Exercise for Simulating Sequences of Earthquakes and Aseismic Slip (SEAS), *Seism. Res. Lett.*, doi:10.1785/0220190248.

Erickson, B. A., E. M. Dunham, and A. Khosravifar (2017), A finite difference method for off-fault plasticity throughout the earthquake cycle, *Journal of the Mechanics and Physics of Solids*, *109*, 50–77.

Erickson, B. A., J. Jiang, V. Lambert, S. D. Barbot, M. Abdelmeguid, M. Almquist, J.-P. Ampuero, R. Ando, C. Cattania, A. Chen, et al. (2023), Incorporating full elastodynamic effects and dipping fault geometries in community code verification exercises for simulations of earthquake sequences and aseismic slip (seas), *Bull. Seism. Soc. Am.*, *113*(2), 499–523, doi:10.1785/0120220066.

Evans, B., and D. L. Kohlstedt (1995), Rheology of rocks, in *Handbook of physical constants. Part 3 - Rock physics and phase relations*, edited by T. J. Ahrens, pp. 148–165, Am. Geophys. Union, Washington, DC.

Faulkner, D., C. Jackson, R. Lunn, R. Schlische, Z. Shipton, C. Wibberley, and M. Withjack (2010), A review of recent developments concerning the structure, mechanics and fluid flow properties of fault zones, *Journal of Structural Geology*, *32*(11), 1557–1575.

Freed, A. M., and J. Lin (2001), Delayed triggering of the 1999 Hector Mine earthquake by viscoelastic stress transfer, *Nature*, *441*, 180–183.

Freed, A. M., T. Herring, and R. Bürgmann (2010), Steady-state laboratory flow laws alone fail to explain postseismic observations, *Earth Planet. Sci. Lett.*, *300*, 1–10.

Fukuda, J., and K. M. Johnson (2021), Bayesian inversion for a stress-driven model of afterslip and viscoelastic relaxation: Method and application to postseismic deformation following the 2011 MW 9.0 Tohoku-Oki Earthquake, *J. Geophys. Res.*, *126*(5), e2020JB021,620, doi:10.1029/2020JB021620.

Gauriau, J., and J. F. Dolan (2021), Relative structural complexity of plate-boundary fault systems controls incremental slip-rate behavior of major strike-slip faults, *Geochemistry, Geophysics, Geosystems*, *22*(11), e2021GC009,938, doi:10.1029/2021GC009938.

Gimbutas, Z., L. Greengard, M. Barall, and T. E. Tullis (2012), On the calculation of displacement, stress, and strain induced by triangular dislocations, *Bull. Seism. Soc. Am.*, *102*(6), 2776–2780.

Hampel, A., and R. Hetzel (2015), Horizontal surface velocity and strain patterns near thrust and normal faults during the earthquake cycle: The importance of viscoelastic relaxation in the lower crust and implications for interpreting geodetic data, *Tectonics*, *34*(4), 731–752, doi:10.1002/2014TC003605.

Hansen, L., M. Zimmerman, and D. L. Kohlstedt (2011), Grain boundary sliding in San Carlos olivine: Flow law parameters and crystallographic-preferred orientation, *J. Geophys. Res.*, *116*(B8), doi:10.1029/2011JB008220.

Heaton, T. H. (1990), Evidence for and implications of self-healing pulses of slip in earthquake rupture, *Phys. Earth Planet. Inter.*, *64*(1), 1–20, doi:10.1016/0031-9201(90)90002-F.

Herrendörfer, R., Y. Van Dinther, T. Gerya, and L. A. Dalguer (2015), Earthquake supercycle in subduction zones controlled by the width of the seismogenic zone, *Nature Geoscience*, *8*(6), 471–474, doi:10.1038/ngeo2427.

Herrendörfer, R., T. Gerya, and Y. Van Dinther (2018), An invariant rate-and state-dependent friction formulation for viscoeastoplastic earthquake cycle simulations, *J. Geophys. Res.*, *123*(6), 5018–5051.

Hetland, E. A., and B. H. Hager (2006), Interseismic strain accumulation: Spin-up, cycle invariance, and irregular rupture sequences, *Geochem. Geophys. Geosys.*, *7*(5), Q05,004.

Hirth, G., and D. L. Kohlstedt (2003), Rheology of the upper mantle and the mantle wedge: a view from the experimentalists, in *Inside the Subduction Factory*, *Geophys. Monogr.*, vol. 138, edited by J. Eiler, pp. 83–105, Am. Geophys. Soc., Washington, D. C., doi:10.1029/138GM06.

Hirth, G., and J. Tullis (1992), Dislocation creep regimes in quartz aggregates, *Journal of Structural Geology*, *14*(2), 145–159.

Hori, T., N. Kato, K. Hirahara, T. Baba, and Y. Kaneda (2004), A numerical simulation of earthquake cycles along the nankai trough in southwest japan: lateral variation in fric-

tional property due to the slab geometry controls the nucleation position, *Earth Planet. Sci. Lett.*, *228*(3-4), 215–226.

Hu, Y., and K. Wang (2012), Spherical-earth finite element model of short-term postseismic deformation following the 2004 sumatra earthquake, *J. Geophys. Res.*, *117*(B5), doi:10.1029/2012JB009153.

Hu, Y., K. Wang, J. He, J. Klotz, and G. Khazaradze (2004), Three-dimensional viscoelastic finite element model for postseismic deformation of the great 1960 Chile earthquake, *J. Geophys. Res.*, *109*(B12403), 14, doi:10.1029/2004JB003163.

Jiang, J., B. A. Erickson, V. R. Lambert, J.-P. Ampuero, R. Ando, S. D. Barbot, C. Cattania, L. D. Zilio, B. Duan, E. M. Dunham, et al. (2022), Community-driven code comparisons for three-dimensional dynamic modeling of sequences of earthquakes and aseismic slip, *J. Geophys. Res.*, *127*(3), e2021JB023,519, doi:10.1029/2021JB023519.

Johnson, K. M., and P. Segall (2004), Viscoelastic earthquake cycle models with deep stress-driven creep along the San Andreas Fault system, *J. Geophys. Res.*, *109*(B10403), doi:10.1029/2004JB003096.

Johnson, K. M., R. Bürgmann, and J. T. Freymueller (2009), Coupled afterslip and viscoelastic flow following the 2002 Denali Fault, Alaska earthquake, *Geophys. J. Int.*, *176*(3), 670–682.

Karato, S., and P. Wu (1993), Rheology of the upper mantle: a synthesis, *Science*, *260*, 771–778, doi:10.1126/science.260.5109.771.

Karato, S.-I., and H. Jung (2003), Effects of pressure on high-temperature dislocation creep in olivine, *Philosophical Magazine*, *83*(3), 401–414, doi:10.1080/0141861021000025829.

Karato, S.-I., M. S. Paterson, and J. D. Fitzgerald (1986), Rheology of synthetic olivine aggregates - Influence of grain size and water, *J. Geophys. Res.*, *91*, 8151–8176, doi:10.1029/JB091iB08p08151.

Kearse, J., and Y. Kaneko (2020), On-fault geological fingerprint of earthquake rupture direction, *J. Geophys. Res.*, *125*(9), e2020JB019,863, doi:10.1029/2020JB019863.

Kirby, S., and A. Kronenberg (1987), Rheology of the lithosphere: Selected topics, *Reviews of Geophysics*, *25*(6), 1219–1244, doi:10.1029/RG025i006p01219.

Kirkpatrick, J. D., and E. E. Brodsky (2014), Slickenline orientations as a record of fault rock rheology, *Earth Planet. Sci. Lett.*, *408*, 24–34, doi:https://doi.org/10.1016/j.epsl.2014.09.040.

Klein, E., L. Fleitout, C. Vigny, and J. Garaud (2016), Afterslip and viscoelastic relaxation model inferred from the large-scale post-seismic deformation following the 2010 m w 8.8 maule earthquake (chile), *Geophysical Journal International*, *205*(3), 1455–1472.

Koch, P. S., J. M. Christie, A. Ord, and R. P. George Jr (1989), Effect of water on the rheology of experimentally deformed quartzite, *J. Geophys. Res.*, *94*(B10), 13,975–13,996.

Kohlstedt, D. L., B. Evans, and S. J. Mackwell (1995), Strength of the lithosphere: Constraints imposed by laboratory experiments, *J. Geophys. Res.*, *100*, 17,587–17,602, doi:10.1029/95JB01460.

Komatitsch, D., and J.-P. Vilotte (1998), The spectral element method: an efficient tool to simulate the seismic response of 2d and 3d geological structures, *Bull. Seism. Soc. Am.*, *88*(2), 368–392.

Lambert, V., and S. Barbot (2016), Contribution of viscoelastic flow in earthquake cycles within the lithosphere-asthenosphere system, *Geophys. Res. Lett.*, *43*(19), 142–154, doi:10.1002/2016GL070345.

Landry, W., and S. Barbot (2016), Gamra: Simple meshing for complex earthquakes, *Computers and Geosciences*, *90*, 49–63, doi:10.1016/j.cageo.2016.02.014.

Landry, W., and S. Barbot (2018), Fast, accurate solutions for 3d strain volumes in a heterogeneous half space, *arXiv preprint arXiv:1802.08931*.

Lapusta, N., and Y. Liu (2009), Three-dimensional boundary integral modeling of spontaneous earthquake sequences and aseismic slip, *J. Geophys. Res.*, *114*(B09303), 25 PP., doi:10.1029/2008JB005934.

Li, D., and Y. Liu (2017), Modeling slow-slip segmentation in cascadia subduction zone constrained by tremor locations and gravity anomalies, *J. Geophys. Res.*, *122*(4), 3138–3157, doi:10.1002/2016JB013778.

Li, S., M. Moreno, J. Bedford, M. Rosenau, O. Heidbach, D. Melnick, and O. Oncken (2017), Postseismic uplift of the andes following the 2010 maule earthquake: Implications for mantle rheology, *Geophys. Res. Lett.*, *44*(4), 1768–1776.

Masuti, S., and S. Barbot (2021), MCMC inversion of the transient and steady-state creep flow law parameters of dunite under dry and wet conditions, *Earth Planets Space*, *73*(1), 1–21, doi:10.1186/s40623-021-01543-9.

Masuti, S., S. Barbot, S. Karato, L. Feng, and P. Banerjee (2016), Upper mantle water stratification inferred from the 2012 Mw 8.6 Indian Ocean earthquake, *Nature*, *538*, 373–377, doi:10.1038/nature19783.

Meade, B. J. (2007), Algorithms for the calculation of exact displacements, strains, and stresses for triangular dislocation elements in a uniform elastic half space, *Comp. Geosc.*, *33*(8), 1064–1075.

Mei, C., S. Barbot, Y. Jia, and W. Wu (2021), Experimental evidence for multiple controls on fault stability and rupture dynamics, *Earth Planet. Sci. Lett.*, *577*, 117,252, doi:10.1016/j.epsl.2021.117252.

Mindlin, R. D. (1936), Force at a point in the interior of a semi-infinite solid, *J. Appl. Phys.*, *7*, 195–202.

Mitchell, E., Y. Fialko, and K. Brown (2016), Velocity-weakening behavior of Westerly granite at temperature up to 600°C, *J. Geophys. Res.*, *121*(9), 6932–6946, doi:10.1002/2016JB013081.

Mitchell, T., and D. Faulkner (2009), The nature and origin of off-fault damage surrounding strike-slip fault zones with a wide range of displacements: A field study from the Atacama fault system, northern Chile, *Journal of Structural Geology*, *31*(8), 802–816, doi:10.1016/j.jsg.2009.05.002.

Miyake, Y., and H. Noda (2019), Fully dynamic earthquake sequence simulation of a fault in a viscoelastic medium using a spectral boundary integral equation method: does interseismic stress relaxation promote aseismic transients?, *Earth Planets Space*, *71*(1), 1–12, doi:10.1186/s40623-019-1113-8.

Moore, J. D., H. Yu, C.-H. Tang, T. Wang, S. Barbot, D. Peng, S. Masuti, J. Dauwels, Y.-J. Hsu, V. Lambert, et al. (2017), Imaging the distribution of transient viscosity after the 2016 Mw 7.1 Kumamoto earthquake, *Science*, *356*(6334), 163–167, doi:10.1126/science.aal3422.

Nakatani, M. (2001), Conceptual and physical clarification of rate and state friction: Frictional sliding as a thermally activated rheology, *J. Geophys. Res.*, *106*(B7), 13,347–13,380, doi:10.1029/2000JB900453.

Nemat-Nasser, S. (2004), *Plasticity. A Treatise on Finite Deformation of Heterogeneous Inelastic Materials*, Cambridge Monographs on Mechanics, Cambridge University Press.

Nemat-Nasser, S., and M. Hori (1999), *Micromechanics: overall properties of heterogeneous materials*, 2 ed., Elsevier.

Nie, S., and S. Barbot (2021), Seismogenic and tremorgenic slow slip near the stability transition of frictional sliding, *Earth Planet. Sci. Lett.*, *569*, 117,037, doi:10.1016/j.epsl.2021.117037.

Nie, S., and S. Barbot (2022), Rupture styles linked to recurrence patterns in seismic cycles with a compliant fault zone, *Earth Planet. Sci. Lett.*, *591*, 117,593, doi:10.1016/j.epsl.2022.117593.

Nield, G. A., M. A. King, R. Steffen, and B. Blank (2022), A global, spherical finite-element model for post-seismic deformation using Abaqus, *Geoscientific Model Development*, *15*(6), 2489–2503, doi:0.5194/gmd-15-2489-2022.

Niemeijer, A., C. Boulton, V. Toy, J. Townend, and R. Sutherland (2016), Large-displacement, hydrothermal frictional properties of DFDP-1 fault rocks, Alpine Fault, New Zealand: Implications for deep rupture propagation, *J. Geophys. Res.*, *121*(2), 624–

647, doi:10.1002/2015JB012593.

Nikkhoo, M., and T. R. Walter (2015), Triangular dislocation: an analytical, artefact-free solution, *Geophys. J. Int.*, *201*(2), 1117–1139.

Noda, H. (2022), Dynamic earthquake sequence simulation with an SBIEM accounting for interseismic poroelastic rebound, *Earth Planets Space*, *74*(1), 1–15, doi:10.1186/s40623-022-01649-8.

Nüchter, J.-A., and S. Ellis (2010), Complex states of stress during the normal faulting seismic cycle: Role of midcrustal postseismic creep, *J. Geophys. Res.*, *115*(B12), doi:10.1029/2010JB007557.

Nur, A., and G. Mavko (1974), Postseismic viscoelastic rebound, *Science*, *183*, 204–206.

Okada, Y. (1985), Surface deformation due to shear and tensile faults in a half-space, *Bull. Seism. Soc. Am.*, *75*(4), 1135–1154.

Okada, Y. (1992), Internal deformation due to shear and tensile faults in a half-space, *Bull. Seism. Soc. Am.*, *82*, 1018–1040.

Okuda, H., A. R. Niemeijer, M. Takahashi, A. Yamaguchi, and C. J. Spiers (2023), Hydrothermal friction experiments on simulated basaltic fault gouge and implications for megathrust earthquakes, *J. Geophys. Res.*, *128*(1), e2022JB025,072, doi:10.1029/2022JB025072.

Ozawa, S., A. Ida, T. Hoshino, and R. Ando (2023), Large-scale earthquake sequence simulations on 3-D non-planar faults using the boundary element method accelerated by lattice H-matrices, *Geophys. J. Int.*, *232*(3), 1471–1481, doi:10.1093/gji/ggac386.

Peltier, W., D. Yuen, and P. Wu (1980), Postglacial rebound and transient rheology, *Geophys. Res. Lett.*, *7*(10), 733–736.

Perez-Silva, A., Y. Kaneko, M. Savage, L. Wallace, D. Li, and C. Williams (2022), Segmentation of shallow slow slip events at the hikurangi subduction zone explained by along-strike changes in fault geometry and plate convergence rates, *J. Geophys. Res.*, *127*(1), e2021JB022,913, doi:10.1029/2021JB022913.

Petrini, C., T. Gerya, V. Yarushina, Y. van Dinther, J. Connolly, and C. Madonna (2020), Seismo-hydro-mechanical modelling of the seismic cycle: Methodology and implications for subduction zone seismicity, *Tectonophysics*, *791*, 228,504, doi:10.1016/j.tecto.2020.228504.

Poirier, J.-P. (1985), *Creep of crystals: high-temperature deformation processes in metals, ceramics and minerals*, Cambridge University Press.

Pollitz, F., P. Banerjee, K. Grijalva, B. Nagarajan, and R. Bürgmann (2008), Effect of 3-D viscoelastic structure on post-seismic relaxation from the 2004 M= 9.2 Sumatra earthquake, *Geophys. J. Int.*, *173*(1), 189–204.

Pollitz, F. F. (1992), Postseismic relaxation theory on the spherical earth, *Bull. Seism. Soc. Am.*, *82*(1), 422–453.

Pollitz, F. F. (1997), Gravitational viscoelastic postseismic relaxation on a layered spherical earth, *J. Geophys. Res.*, *102*, 17,921–17,941.

Pollitz, F. F. (2003a), Transient rheology of the uppermost mantle beneath the Mojave Desert, California, *Earth Planet. Sci. Lett.*, *215*(1-2), 89–104.

Pollitz, F. F. (2003b), Post-seismic relaxation theory on a laterally heterogenous viscoelastic model, *Geophys. J. Int.*, *155*, 55–78.

Pollitz, F. F. (2019), Lithosphere and shallow asthenosphere rheology from observations of post-earthquake relaxation, *Phys. Earth Planet. Inter.*, *293*, 106,271, doi:10.1016/j.pepi.2019.106271.

Pollitz, F. F., G. Peltzer, and R. Bürgmann (2000), Mobility of continental mantle: Evidence from postseismic geodetic observations following the 1992 landers earthquake, *J. Geophys. Res.*, *105*(B4), 8035–8054, doi:10.1029/1999JB900380.

Pollitz, F. F., C. Wicks, and W. Thatcher (2001), Mantle Flow Beneath a Continental Strike-Slip Fault: Postseismic Deformation After the 1999 Hector Mine Earthquake, *Science*, *293*, 1814–1818.

Pollitz, F. F., R. Bürgmann, and P. Banerjee (2006), Post-seismic relaxation following the great 2004 Sumatra-Andaman earthquake on a compressible self-gravitating Earth, *Geophys. J. Int.*, *167*(1), 397–420.

Post, R. L. (1977), High-temperature creep of mt. burnet dunite, *Tectonophysics*, *42*, 75–110.

Press, F. (1965), Displacements, strains, and tilts at teleseismic distances, *J. Geophys. Res.*, *70*(10), 2395–2412.

Press, W. H., S. A. Teukolsky, W. T. Vetterling, and B. P. Flannery (1992), *Numerical Recipes in C: The Art of Scientific Computing*, 2nd ed., 994 pp., Cambridge Univ. Press, New York.

Qiu, Q., E. M. Hill, S. Barbot, J. Hubbard, W. Feng, E. O. Lindsey, L. Feng, K. Dai, S. V. Samsonov, and P. Tapponnier (2016), The mechanism of partial rupture of a locked megathrust: The role of fault morphology, *Geology*, *44*(10), 875–878, doi:10.1130/G38178.1.

Qiu, Q., J. D. P. Moore, S. Barbot, L. Feng, and E. Hill (2018), Transient Viscosity in the Sumatran Mantle Wedge from a Decade of Geodetic Observations, *Nature Communications*, *9*(995), doi:10.1038/s41467-018-03298-6.

Ranalli, G. (1980), Transient creep in the upper mantle, *Il Nuovo Cimento C*, *3*(4), 405–419.

Rice, J. R., and S. T. Tse (1986), Dynamic motion of a single degree of freedom system following a rate and state dependent friction law, *J. Geophys. Res.*, *91*(B1), 521–530.

Rollins, C., S. Barbot, and J.-P. Avouac (2015), Postseismic deformation following the 2010 M=7.2 El Mayor-Cucapah earthquake: Observations, kinematic inversions, and dynamic models, *Pure Appl. Geophys.*, *172*(5), 1305–1358, doi:10.1007/s00024-014-1005-6.

Romanet, P., and S. Ozawa (2022), Fully dynamic earthquake cycle simulations on a nonplanar fault using the spectral boundary integral element method (sbiem), *Bull. Seism. Soc. Am.*, *112*(1), 78–97, doi:10.1785/0120210178.

Romanet, P., H. S. Bhat, R. Jolivet, and R. Madariaga (2018), Fast and slow slip events emerge due to fault geometrical complexity, *Geophys. Res. Lett.*, *45*, 4809–4819.

Rousset, B., S. Barbot, J. P. Avouac, and Y.-J. Hsu (2012), Postseismic Deformation Following the 1999 Chi-Chi Earthquake, Taiwan: Implication for Lower-Crust Rheology, *J. Geophys. Res.*, *117*(B12405), 16, doi:10.1029/2012JB009571.

Rutter, E., and K. Brodie (2004), Experimental grain size-sensitive flow of hot-pressed Brazilian quartz aggregates, *Journal of Structural Geology*, *26*(11), 2011–2023, doi:10.1016/j.jsg.2004.04.006.

Rybacki, E., and G. Dresen (2000), Dislocation and diffusion creep of synthetic anorthite aggregates, *J. Geophys. Res.*, *105*(B11), 26,017–26,036.

Sathiakumar, S., and S. Barbot (2021), The stop-start control of seismicity by fault bends along the Main Himalayan Thrust, *Communications Earth & Environment*, *2*(1), 1–11, doi:10.1038/s43247-021-00153-3.

Savage, J. (2000), Viscoelastic-coupling model for the earthquake cycle driven from below, *J. Geophys. Res.*, *105*(B11), 25,525–25,532.

Segall, P. (2010), *Earthquake and volcano deformation*, Princeton University Press, Princeton, NJ.

Shea, W. T., and A. K. Kronenberg (1992), Rheology and deformation mechanisms of an isotropic mica schist, *J. Geophys. Res.*, *97*(B11), 15,201–15,237, doi:10.1029/92JB00620.

Shi, P., M. Wei, and S. Barbot (2022), Contribution of viscoelastic stress to the synchronization of earthquake cycles on oceanic transform faults, *J. Geophys. Res.*, *127*(8), e2022JB024,069, doi:10.1029/2022JB024069.

Shi, Q., S. Barbot, B. Shibazaki, T. Matsuzawa, S. Wei, and P. Tapponnier (2020), Structural control and system-level behavior of the seismic cycle at the Nankai trough, *Earth Planets Space*, *72*(1), 1–31, doi:10.1186/s40623-020-1145-0.

Shibazaki, B., and T. Shimamoto (2007), Modelling of short-interval silent slip events in deeper subduction interfaces considering the frictional properties at the unstable/stable transition regime, *Geophys. J. Int.*, *171*(1), 191–205.

Shibazaki, B., T. Matsuzawa, and A. Tsutsumi (2011), 3D modeling of the cycle of a great Tohoku-oki earthquake, considering frictional behavior at low to high slip velocities, *Geophys. Res. Lett.*, *38*(L21305), doi:10.1029/2011GL049308.

Shibazaki, B., L. M. Wallace, Y. Kaneko, I. Hamling, Y. Ito, and T. Matsuzawa (2019), Three-dimensional modeling of spontaneous and triggered slow-slip events at the hikurangi subduction zone, new zealand, *J. Geophys. Res.*, *124*(12), 13,250–13,268, doi:10.1029/2019JB018190.

Smith, B., and D. Sandwell (2004), A three-dimensional semianalytic viscoelastic model for time-dependent analyses of the earthquake cycle, *J. Geophys. Res.*, *109*, doi:10.1029/2004JB003185.

Sobolev, S. V., and I. A. Muldashev (2017), Modeling seismic cycles of great megathrust earthquakes across the scales with focus at postseismic phase, *Geochemistry, Geophysics, Geosystems*, *18*(12), 4387–4408, doi:10.1002/2017GC007230.

Suito, H., and J. T. Freymueller (2009), A viscoelastic and afterslip postseismic deformation model for the 1964 Alaska earthquake, *J. Geophys. Res.*, *114*(B11404), 23.

Sun, T., K. Wang, T. Iinuma, R. Hino, J. He, H. Fujimoto, M. Kido, Y. Osada, S. Miura, Y. Ohta, and Y. Hu (2014), Prevalence of viscoelastic relaxation after the 2011 Tohoku-oki earthquake, *Nature*, *514*, 84–87, doi:10.1038/nature13778.

Tada, T. (2009), Boundary integral equation method for earthquake rupture dynamics, *International Geophysics*, *94*, 217–267, doi:10.1016/S0074-6142(08)00009-0.

Takeuchi, C. S., and Y. Fialko (2013), On the effects of thermally weakened ductile shear zones on postseismic deformation, *J. Geophys. Res.*, *118*(12), 6295–6310.

Tanaka, Y., T. Hasegawa, H. Tsuruoka, V. Klemann, and Z. Martinec (2015), Spectral-finite element approach to post-seismic relaxation in a spherical compressible Earth: application to gravity changes due to the 2004 Sumatra–Andaman earthquake, *Geophys. J. Int.*, *200*(1), 299–321, doi:10.1093/gji/ggu391.

Tang, C.-H., Y.-J. Hsu, S. Barbot, J. D. Moore, and W.-L. Chang (2019), Lower-crustal rheology and thermal gradient in the Taiwan orogenic belt illuminated by the 1999 Chi-Chi earthquake, *Nature Communications*, *5*(2), doi:10.1126/sciadv.aav3287.

Tang, C.-H., S. Barbot, Y.-J. Hsu, and Y.-M. Wu (2020), Heterogeneous power-law flow with transient creep in southern California following the 2010 El Mayor-Cucapah earthquake, *J. Geophys. Res.*, *125*(9), e2020JB019,740, doi:10.1029/2020JB019740.

Thieme, M., S. Demouchy, D. Mainprice, F. Barou, and P. Cordier (2018), Stress evolution and associated microstructure during transient creep of olivine at 1000–1200°C, *Physics of the Earth and Planetary Interiors*, *278*, 34–46.

Tokle, L., G. Hirth, and W. M. Behr (2019), Flow laws and fabric transitions in wet quartzite, *Earth Planet. Sci. Lett.*, *505*, 152–161, doi:10.1016/j.epsl.2018.10.017.

Van Zelst, I., S. Wollherr, A.-A. Gabriel, E. H. Madden, and Y. van Dinther (2019), Modeling megathrust earthquakes across scales: One-way coupling from geodynamics and seismic cycles to dynamic rupture, *J. Geophys. Res.*, *124*(11), 11,414–11,446, doi:10.1029/2019JB017539.

Veedu, D. M., C. Giorgetti, M. Scuderi, S. Barbot, C. Marone, and C. Collettini (2020), Bifurcations at the stability transition of earthquake faulting, *Geophys. Res. Lett.*, *47*(19), e2020GL087,985, doi:10.1029/2020GL087985.

Wang, B., and S. Barbot (2023a), Pulse-like ruptures, seismic swarms, and tremorgenic slow-slip events with thermally activated friction, *Earth Planet. Sci. Lett.*, *603*, 117,983, doi:10.1016/j.epsl.2022.117983.

Wang, K. (2007), Elastic and viscoelastic models of crustal deformation in subduction earthquake cycles, *The seismogenic zone of subduction thrust faults*, pp. 540–575.

Wang, K., Y. Hu, and J. He (2012), Deformation cycles of subduction earthquakes in a viscoelastic earth, *Nature*, *484*(7394), 327.

Wang, L., and S. Barbot (2020), Excitation of San Andreas tremors by thermal instabilities below the seismogenic zone, *Science Advances*, *6*(36), eabb2057, doi:10.1126/sciadv.abb2057.

Wang, L., and S. Barbot (2023b), Three-dimensional kinematics of the India–Eurasia collision, *Comm. Earth & Env*, *4*(164), doi:10.1038/s43247-023-00815-4.

Wang, R., F. Martin, and F. Roth (2003), Computation of deformation induced by earthquakes in a multi-layered elastic crust - FORTRAN programs EDGRN/EDCMP, *Comp. Geosci.*, *29*, 195–207.

Wang, R., S. Heimann, Y. Zhang, H. Wang, and T. Dahm (2017), Complete synthetic seismograms based on a spherical self-gravitating earth model with an atmosphere–ocean–mantle–core structure, *Geophysical Journal International*, *210*(3), 1739–1764, doi:10.1093/gji/ggx259.

Weiss, J. R., Q. Qiu, S. Barbot, J. H. Foster, T. J. Wright, A. Saunders, B. A. Brooks, M. Bevis, E. Kendrick, R. S. Jr., S. R. Cimbaro, L. E. Lenzano, J. Barón, J. C. Báez, A. Echalar, and J. Avery (2019), Illuminating subduction zone rheological properties in the wake of a giant earthquake, *Sci. Adv.*, doi:10.1126/sciadv.aax6720.

Zhang, H., and X. Chen (2006), Dynamic rupture on a planar fault in three-dimensional half space—i. theory, *Geophys. J. Int.*, *164*(3), 633–652, doi:10.1111/j.1365-246X.2006.02887.x.

Zhang, X., and T. Sagiya (2018), Intraplate strike-slip faulting, stress accumulation, and shear localization of a crust-upper mantle system with nonlinear viscoelastic material, *J. Geophys. Res.*, *123*(10), 9269–9285, doi:10.1029/2018JB016421.